Leveraging Stereolithography-enabled 3D Printing for Biomimetic Microfluidic Advancements

by

Jessica Hallgath

A thesis submitted in partial fulfillment
of the requirements for the degree of
Master of Science in Engineering
(Bioengineering)
in the University of Michigan-Dearborn
2019

Master's Thesis Committee:

Associate Professor Joe Fu-Jiou Lo, Chair
Professor Ben Q. Li
Assistant Professor Tanjore V. Jayaraman
Assistant Professor Mathumai Kanapathipillai

Acknowledgements

I would first like to extend my thanks to Dr. Joe Lo for his guidance and mentorship in the completion of my thesis and graduate degree. I am thankful for the laboratory training provided to me by Kai Duan and Luwei Zou. I am thankful to Zachary Bustamante, Kai Duan and Hussam Mawari for their assistance in aspects of this thesis. I am thankful for the collaboration with Dr. Mark Cheng and student Boshen Zhang (Wayne State University). Further gratitude is extended to lab members Dr. Aref, Siyu Chen, Samer Habeel, Suhaib Hashem, Eiji Isomura, and the laboratory members of Dr. Argento, Dr. Chakraborty, Dr. Ghosh, and Dr. Kanapathipillai for their friendship and support throughout my research. I would also like to acknowledge the support from the following grant sources:

NSF 175142, "CAREER: Probing Mechanisms of Beta Cell Dysfunction via Quantitative Droplet Molecular Transport"

NIH NIBIB, R03 award, R03EB023459, "Probing Hypoxia and Fatty Acid Synergy in Beta Cell Impairments via Multimodal Microfluidics"

Table of Contents

List of Figures

List of Tables

List of Abbrievations

CNT	Carbon nanotube
DLP	Dynamic Light Processor
ID	Inner diameter
IPA	Isopropyl alcohol
LOC	Lab-on-a-chip
MEMS	Micro-ElectroMechanical System
NA	Numerical Aperture
PDMS	Polydimethylsiloxane
PLA	Polylactic acid
PSP	Passive Self Peeling
RBCs	Red blood cells
RPM	Rotations per minute
SLA	Stereolithography
μTesla	Microscale Tesla Pump
UV	Ultraviolet
Vat	Refers to the PSP Resin container (Kudo3D Titan 2 DLP SLA Printer)
WBCs	White blood cells

Abstract

This thesis represents three major efforts in applying microscale additive manufacturing to address bioengineering applications. Additive manufacturing entails using basic building blocks to construct the three-dimensional structure of a device, affording rapid prototyping and lower costs in research and development. Here, a digital light processor (DLP) based stereolithography 3D printing system is leveraged to achieve microscale resolutions for devices. The first application creates microelectromechanical systems (MEMS) geometries for biosensors and biomimetic optics. The second application is to realize an integrated micro Tesla (μTesla) pump in a microfluidic platform. The third application is to optimize the fluid-surface coupling in the μTesla rotors to pump differential viscosities, including shear-thinning viscosities. These efforts span across Biosensors, Biomicrofluidics, and Biotransport and demonstrate 3D printing as a key enabling technology to improve bioengineering instrumentation.

In the first part, MEMS interface with biology to create simplistic models of complex natural phenomena. In this work, 3D printing is used to create a microscale fabrication platform for carbon nanotube (CNT) proliferation. In a parallel work, the 3D printing aids in defining microoptic dimensions of a biomimetic compound eye element previously unattainable via traditional fabrication.

In the second part, studies of biological phenomena can be augmented by microfluidic devices to model native physiological conditions at the microscale level. When studying the effect of shear stress and transport on beta cells in diabetes mechanisms, the need for an

integrated, microscale flow source arose. This work introduces the μTesla pump as a flow source for lab-on-a-chip (LOC) applications. The experimental results demonstrate the μTesla pump's capacity to generate highly controllable shear stress. Moreover, this work demonstrates the ability to fine-tune 3D printed surface characteristics to optimize pressure output of the system.

Lastly, the pump's capability to pump blood analog fluids is analyzed. Pumping of shear thinning fluid is investigated. This portion of the thesis aims to define the parameters of biofluids both from device perspective as well as pathophysiological perspectives through experimentation and modeling. Understanding gained in this thesis should help to model blood shear at the capillary level, a model for a number of diabetes and cardiovascular related diseases.

Chapter 1. Stereolithography-Enabled Additive Manufacturing

Motivation

The motivation for this work came from a need for finely tuned flow source for lab-on-a-chip models, specifically the reaction of pancreatic beta cells to shear forces in diabetes pathophysiology. μTesla flow was characterized for a variety of conditions to determine optimal fluid/pump coupling for pumping of biological fluids. Moreover, other biosensors and biomimetic solutions were improved upon through 3D printing optimization.

Introduction

In contemporary technology, additive manufacturing (AM) is a rapidly progressing field finding a home in academics, industry, and cutting-age research. AM refers to an entire family of processes in which the product is produced from the bottom up, meaning that smaller building blocks join to produce a final product. AM works in direct opposition to historically-driven top down processes such as CNC machining or carving in which material is removed from a larger substrate. Due to the advent of numerous user-friendly AM softwares, AM is replacing a lot of top down processes in industry owing to its ease of use for rapid prototyping and/or high customization capacity for highly specific end-products.

One of the most visible technologies within the AM field is 3D printing. While society places emphasis on the more rare, problematic applications of 3D printed biological tissues or organs[1,2]; 3D printing has already found its home in numerous medical capacities such as surgical planning tools[3] or patient specific joint replacement solutions[4]. “3D printing” itself

refers to a larger family of technologies, the most visible being the extrusion-based softwares such as those manufactured by MakerBot[5]. Extrusion-based 3D printing usually utilizes environmentally safe plastic filament (such as PLA) which, when heated, can be extruded into a pre-planned pattern. While extrusion-based 3D printing is inarguably the most widely known technology, the scientific research community can be quick to point out its drawbacks such as the limitations imposed by extrusion material. For the purposes of microfluidic research, we turn to a different AM technology called stereolithography-enabled (SLA) 3D printing. The driving force behind this decision is the ability of SLA to produce high resolution prints with final dimensions on the millimeter scale. As will be discussed in future chapters of this work, the end product quality of SLA printing is not only advantageous to microfluidic studies, but also to biomimetic research solutions.

Kudo3D Titan 2 DLP SLA Printer

Formlabs, a notable SLA manufacturer, defines stereolithography as "technology that converts liquid materials into solid parts, layer by layer, by selectively curing them using a light source in a process called photopolymerization[6]. The work produced here utilizes the Kudo3D Titan 2 DLP SLA[7] printer. As seen in Figure 1, the Titan 2 features a large black base that houses a DLP projector. The projector yields a 50 μm resolution image onto the clear container. The black stage raises up throughout the print to create the final product, in Figure 1, the Statue of Liberty.

The Titan 2 printer was chosen for this work in large part due to Kudo3D's patented passive self-peeling (PSP) technology. In SLA based printing, the image is exposed through the photo-active resin onto the stage. After a certain amount of exposure time, the stage is raised about 15 mm to remove extra, unexposed resin before the stage is returned to the lower height

and the next layer is projected. This process is repeated until each layer is completed. For our prints, a layer height of 50 μm is used, and thus each time the stage returns to the lower position, it is 50 μm higher than the previous layer. The PSP technology is greatly advantageous in this process. When the stage is lifted out of the resin, a small vacuum force is created. This can cause a variety of problems, especially for millimeter scale prints. For example, if the vacuum force is too large, it may remove the exposed layers from the stage, ruining prints.

Figure 1. Kudo3D Titan 2 Printer

The PSP resin containers are rectangular receptacles made of plastic. The bottom of the vat and shorter edges of the rectangle are made of hard plastic. As seen in Figure 2, there is a plastic edge that sits under a metal bar to hold that edge of the vat in place, but the other edge is free moving to rise with the stage due to vacuum forces. The longer edges of the vat are composted of more flexible plastic to allow for this movement.

Figure 2. Kudo3D PSP Resin Technology

The most important aspect of this PSP resin container is present on the bottom surface. The bottom of the container features a soft silicone material with a Teflon film attached passively to serve as a barrier between the

silicone and the resin. This technology minimizes the effect high separation forces on the print when the stage is moves up and down. It allows for the vat to separate fully and return to the neutral position before the stage returns for the next image exposure. Overall, this allows for higher resolution on the micron scale as necessary for microfluidic and biomimetic applications.

Methods

Much of my research required extensive operating knowledge of this particular machine and learning to troubleshoot any discrepancies in expected results. The general workflow of producing a 3D print is as follows:

Loading a Design

The 3D printer requires that all CAD files be converted to .stl files. This can be done under "save as" in the original CAD program (i.e. CATIA, AutoCAD Inventor). If the object needs to be edited in any way such as requiring printing supports/base, or needs to be rotated, cut in half, duplicated, etc., it will need to be opened in Meshmixer. After the model is finalized, it must be uploaded to the program SLAcer. This will slice the design into the appropriate number of slices. SLAcer will slice the model and generate a zip file. The zip file must be checked to ensure that the slices will print properly. Once the slices have been verified for accuracy, the file is uploaded to the Kudo3D interface.

Preparing to Print

Once the print file is uploaded to the Kudo3D interface and opened, printing parameters must be established. There are a variety of parameters that can be edited on the interface, such as lift height and speed. Kudo3D provides a general guideline for these parameters, but many customized settings have been required to print the highly specific designs detailed in this work.

There also exists a fair amount of physical preparation for the Titan 2 machine. First, the PSP resin container must be selected. There are two main types of vats, “hard” vats, with stiffer silicone bottoms, and “soft” vats with less stiff silicone bottoms. Most prints referenced in this work utilize the hard vat, as it has a higher capacity for producing flat surfaces. Next, the vat must be clean. The bottom of the vat is wiped with methanol to ensure it does not have any resin residue from previous prints. The top of the 3D printer where the vat will sit is also wiped. The vat is inserted on the top of the 3D printer. The vat should rest flat on the top of the printer.

Next, the stage on which the print will be projected is selected. The Titan 2 comes with two types of stages: a porous stage and a solid stage. The porous stage usually works best as it decreases vacuum forces, but it does have the potential to alter prints that do not have a disposable printing base. The stage is cleaned by wiping any resin residue away with isopropyl alcohol (IPA). The zero plane for the stage must be calibrated to ensure that the stage itself is flat when it reaches the bottom of the vat. The stage calibration can be checked by placing a piece of paper between the stage and the bottom of the resin container. When the stage is in appropriate down position, the piece of paper should be tough to pull out, but not impossible (it should not rip). After everything is physically calibrated, the resin should be poured to cover the bottom of the vat completely. Before starting the print, the room should be dark (or the light blocking cover should be utilized) to avoid extraneous exposure of the resin.

Post-processing

The length of time a print takes is directly proportional to the number of layers of the print, including the necessary exposure times and lifting height between layers. For the purposes of this research, most prints take between 30 and 90 minutes to complete. After the print is finished, it is washed with IPA. Once most of the loose resin is washed away, the print is gently

removed from the stage using a razor blade. The print is then submerged in IPA and placed in the sonicator for a few minutes to ensure all the resin is washed away. Next, the print is submerged in a dish of water and placed under the UV lamp for 5-10 minutes for post curing. The printing stage and resin vat are cleaned and/or prepared for the next print.

This basic methodology has adapted over the course of the last two years to complete specific projects. Much troubleshooting was and continues to be required as the Titan 2 printer is used for a variety of applications.

Chapter 2. 3D Printed Biomimetic Solutions

Introduction

The biomedical engineering research community is constantly in search of innovative ways to address complex human problems while minimizing the need for biological tissue. While research involving human tissue or live animal will always be necessary for Food and Drug Administration approved solutions, a lot of rudimentary level research can benefit from biomimetic solutions to not only reduce the use of live tissues, but also reduce required cost to the researcher. Biomimetics refers to the study or development of solutions that mimic or build off of natural biological systems and/or processes[8]. Some of this research yields high level industrial solutions such as the replication of the human brain's neural networks for use in artificial intelligence[9], while other aspects of this research allow for man-made organ models to be used in pharmacological testing, decreasing the need for animal models at early research stages[10, 11, 12].

While the vast majority of this work represents a highly mechanical study of fluid flow over 3D printed surfaces, the necessity of the study was born of a desire to solve biological problems. Thus, the following chapter details a few projects rooted in biomimetic solutions that are improved upon by my expertise in SLA-enabled 3D printing.

3D Print Enabled Biomimetic Compound Eye

Dr. Mark Cheng[13] of Wayne State University is an electrical engineer with research focuses on biomedical microdevices, microelectromechanical systems (MEMS) and nanomanufacturing, among other interests. In a collaboration with his laboratory and one of his doctoral students, Boshen Zhang, I have worked to fine tune the 3D printer for the application of a biomimetic compound eye. The term "compound eye" differs from the human "camera eye" by compartmentalizing the necessary sight components – lens, retina and pigment. These types of eyes are seen in many small animals such as crustaceans and insects, including the widely known drosophila, Figure 3[14]. In this model, the cornea requires a cylindrical lens, but later shifts to a hexagonal shape to house photoreceptors in a unit called the ommatidia.

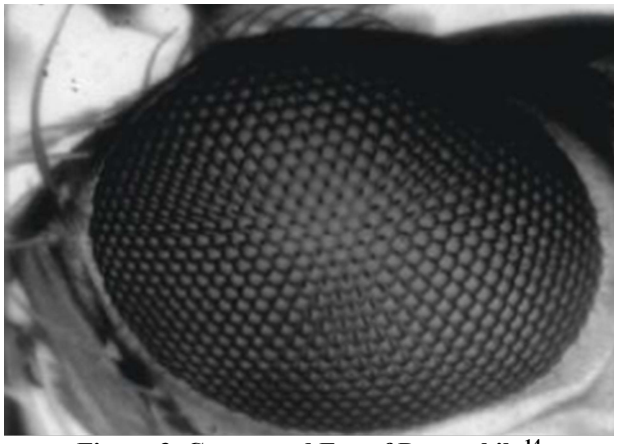

Figure 3. Compound Eye of Drosophila[14]

This 3D print consists of a group of 200 μm internal diameter cylindrical holes. The cylinder openings are circular on one end and hexagonal on the other. The resolution of these prints is crucial as the cylinders will be filled with a polymer for use as a lens. The surface of curvature of a lens is highly important due to Snell's law[15]. Electromagnetic light energy and momentum must be conserved as the light ray crosses into a new medium. Snell's law states that the angle of incidence times the refractive index of the material will be directly proportional to

the angle of the refracted ray times the refractive index of the new material. Velocity of the ray will increase or decrease as necessary. Regardless, it is clear that the interface between the two materials is crucial for the expected physical phenomena to occur. If the interface is expected to be circular but is actually oval due to limitations of the 3D print, the expected physical properties of the lens will not be obtained. If the proper lens shape is not obtained, the numerical aperture (NA) will be reduced, reducing the amount of light the lens accepts and complicating experimental procedures. Thus, it is crucial that the 3D print be void of mistakes.

When printing this design, it was initially difficult to obtain the hexagonal pattern with sufficient accuracy. My experience with 3D printing allowed for a solution to this problem (Figure 4). When orienting a computer-generated model for 3D printing, it is often desirable to print in such a way that the least amount of print layers will be required and such that the amount of unsupported structures is minimized. However, as previously stated, vacuum forces exist when separating the print platform from the resin vat. In the case of the compound eye model, the ideal print orientation would place the open cylindrical holes parallel to the stage. However, since the cylindrical/hexagonal openings were so small and required high resolution, this method proved ineffective. The resin could not properly drain from the cylinders, leading to extraneous resin exposure and diminishing the resolution of the print. The extraneously exposed portions of this design led to inconsistent cylindrical diameters and did not allow for the hexagonal openings to resolve. The combination of these factors led to spherical aberrations when attempting to insert the polymer for biomimetic lens applications.

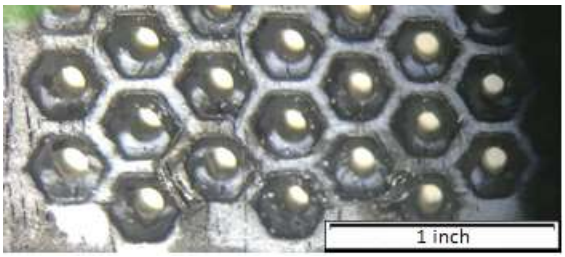

Figure 4. Hexagonal to Cylindrical Opening Interface

Counterintuitively, this print had to be printed on a 90° rotation for optimal results. This orientation did not minimize the amount of print layers or unsupported structures, but instead allowed for greater separation between cured and uncured resin, a parameter that proved vital for long-term results. Figure 4 shows a successful print at a slight angle to better visualize the connection between the hexagonal and cylindrical shape.

Fabrication Platform

Another aspect of the collaboration with Dr. Cheng's laboratory is the creation of a platform for carbon nanotube (CNT) formation. The presence of CNTs in biosensors continues to increase. They are able to act as immunosensors and nucleic acid sensing devices. Furthermore, they are able to amplify electron transport in bioreactions[41]. This platform consists of many pillars, as seen in Figure 5. These pillars range in diameter from 50 μm to 500 μm and range in height from 1 cm to 4 cm. One main goal of this work is to demonstrate the large aspect ratio made possible by 3D printing. Many iterations of these designs were performed due to their small size. Though the Kudo3D Titan 2 printer boasts 50 μm resolution, it can be difficult to achieve this resolution if the printer is not consistently used in this capacity. The everyday operations of this machine were to create pieces that were much bigger and thus adapting to this small size introduced a problem in need of an engineering solution.

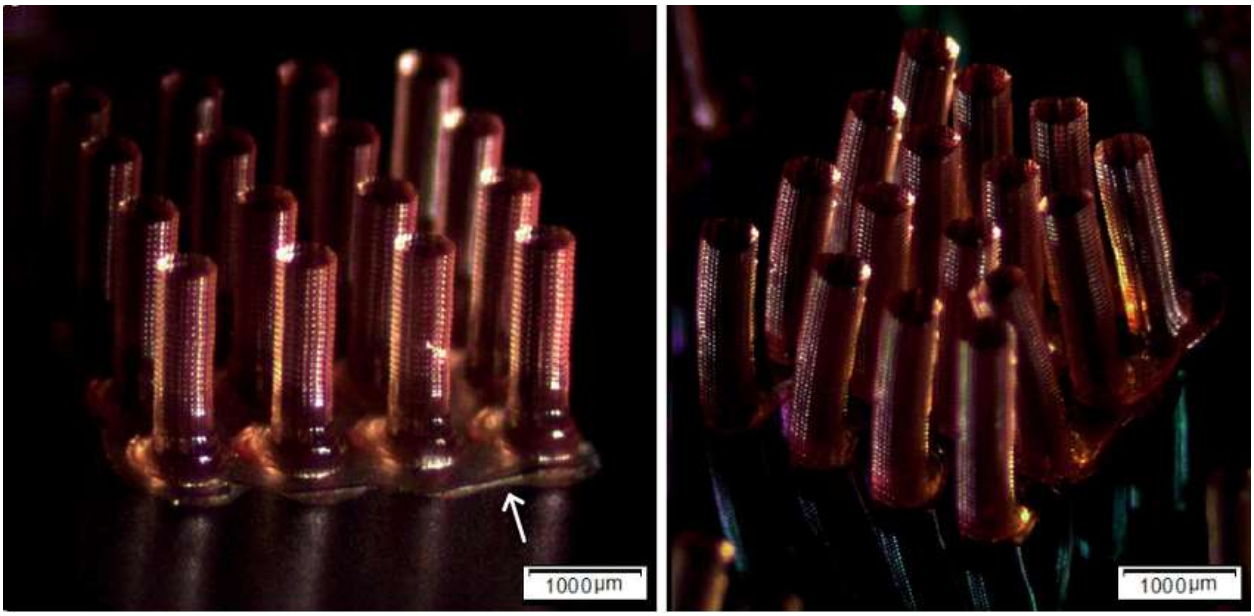

Figure 5. Micro Pillar Array

As mentioned in Chapter 1, the Kudo3D team provides a set of printing parameters that can be employed for almost any print. The parameters were unable to be applied successfully to this model. To print this structure, I had to re-optimize the protocol for printing to be specifically tailored to the geometry that Dr. Cheng's student had designed.

As seen in Figure 6 below, the modification I developed involved variations of exposure time (sec), lift height (mm), and lift speed (mm/s). Down speed (mm/s) and delay time (sec) were not adjusted because they have no direct correlation to print quality. The "from layer" and "to layer" were also left unchanged. Altering these parameters would introduce a lot of unnecessary risk for very little reward. The likelihood of a print's success being dependent on a few layers is very low, and it is easier to trust that Kudo3D has separated the layers properly. As shown, the first layer receives an individualized treatment to ensure initial bonding to the substrate. The following 29 layers are also treated with more caution before spending less time on any remaining layers. Thus, modifications were only made to the exposure time, lift height, and lift speed of the program.

From Layer	To Layer	Exp. Time	Lift Height	Lift Speed	Down Speed	Delay Time
1	1	20	5	15	150	0.5
2	9	10	4	15	150	0.5
10	20	8	3	15	150	0.5
21	30	6	2	15	150	0.5
31	80	5	1.5	15	150	0.5
81	140	2.8	1.2	15	150	0.5

Original Parameters

From Layer	To Layer	Exp. Time	Lift Height	Lift Speed	Down Speed	Delay Time
1	1	18	9	18	150	0.5
2	9	13	9	17	150	0.5
10	20	7	9	17	150	0.5
21	30	6	5	15	150	0.5
31	80	5	2.5	15	150	0.5
81	140	2.8	1.2	15	150	0.5

Modified Parameters

Figure 6. Modification of Printing Parameters

Initial exposure time is high (20 seconds pre-modification) to ensure the print is fully attached to the substrate. For the pillar array, the initial exposure time had to be decreased. This is because resin was also becoming exposed between the pillars, leaving a thin film connection between the pillars (as indicated by the white arrow in Figure 5). This was unacceptable to our collaborators as they needed to heat the 3D prints to an extremely high temperature. If the thin film was present, the pillars would warp together instead of remaining separate entities. Thus, the exposure time was decreased to avoid thin film formation, but still needed to be high enough to ensure bonding to the substrate. Bonding was ensured through the use of an SU-8 coating to act as an adhesion layer on top of the bare silicon wafer. The wafer was attached to the print stage using hot glue, with the SU-8 adhesion coating in place. Exposure time for subsequent print layers was also decreased to avoid extraneous resin exposure.

Lift height was increased for the first 80 layers of printing. An increase in lift height will make the stage rise higher between layers, allowing more time for extra resin to drip and

ensuring the print separates from the vat. However, this also increases total print time, so lift height should be minimized when possible. Due to the small features, it was essential to increase lift height. The increase in lift height for the first 20 layers is drastic. Before modification, it sometimes seemed as if layers of the print were "missing", and thus it was desirable to ensure that more time was spent perfecting these layers.

Lastly, lift speed was also increased for the first 20 layers. In general, if the print is rising too slowly, it may be unable to overcome attractive surface forces and may fall off the platform. However, for very small prints, lift speed cannot be too high as it may cause smaller features to be lost. The increase in lift speed helped to ensure that the extraneous resin was removed from the very small spaces between the pillars.

As demonstrated, the collaboration with Wayne State extended my knowledge of the Kudo3D Titan 2 DLP SLA system. This knowledge proved essential for the success of our laboratory and was also beneficial in producing prints necessary for the μTesla pump.

3D Print Enabled Lab-on-a-Chip Solutions

One of the most common applications of microfluidic platforms is to create a LOC model[10, 11, 12]. These models allow researchers to replicate human body systems on a small scale and provide insight into how a biological system would react to a pharmacological intervention or a specific type of fluid flow. Moreover, lab on a chip systems can provide more than biological mimicry. Through a variety of inertial flow manipulations, lab on a chip systems can perform molecular sorting or droplet generation.

As a member of a laboratory studying microfluidics, it is not surprising that much of this research was born of need for a microfluidic device. Microfluidic principles can be seen in

glucometers or any other lateral flow devices. Using microscale channels, a microfluidic device can more closely mimic naturally occurring body systems and is able to minimize the use of reagents leading to cost reduction. Dr. Leary confirms this information, adding that microfluidics allows for a detailed analysis of a single cell and can even hold imaging capabilities[16].

As lab on a chip systems continue to provide cutting edge research solutions, there is an increasing need for supplemental microscale components to help these solutions reach their full potential. For example, a small-scale imaging device could someday replace the need of a high-power microscopy device for result readout. Another supplemental component of microfluidic systems of interest in this work is that of a compact fluid flow generator. My work this area is detailed in the following sections and provides a natural segue into the bulk of this work (Chapters 3-6).

Diabetic Pathophysiology as an Inspiration for μTesla Pump

Despite its worldwide prevalence, the pathophysiology surrounding type II diabetes is not well understood. Of particular interest is that while type II diabetes is often associated with obesity, not all obese patients have diabetes. Furthermore, not all diabetic patients are obese. Therefore, it can be theorized that there exists an underlying mechanism, or synergy of mechanisms that contribute to the development of type II diabetes. We believe there is possible synergy between the presence of free fatty acids and hypoxic conditions in the pancreas – both known to prematurely stimulate the release of insulin – as a mechanism for diabetes development[17]. Work in our laboratory seeks to characterize the response of beta cells to highly specific environmental conditions through experiments using novel microfluidic platforms as specified in the NSF Career Grant received by Dr. Joe Lo. One of the microfluidic devices utilized in these experiments is a gas gradient generator. The device consists of an inlet and

outlet for oxygen. The oxygen flows through multiple smaller channels as seen in Figure 7. On the opposing side, nitrogen is diffused through the channels, allowing an oxygen gradient to form. At this stage in the experimentation, this device was used to perform live-dead assays of beta cells when exposed to different oxygen concentrations as generated by the gradient.

One requirement of these microfluidic platforms is that the fluid flow is generated by a reliable pump known to produce highly specific flows. Moreover, the ability to encase a micropump inside of a device itself (as opposed to exterior syringe or peristaltic pumping systems) will allow for continuous and contained cell culture. The μTesla pump was seen as a solution to the problems faced in accomplishing preliminary goals toward this diabetic pathophysiology research[18]. A large amount of time (Chapters 4-6) was required to fully characterize the μTesla pump for these purposes, and thus less progress than initially expected was made regarding the characterization of the beta cells themselves. The contribution I have been able to make toward the NSF grant research includes the preparation of beta cells for experimentation and the preparation of microfluidic devices for live-dead assay and is detailed in the following Materials and Methods sections.

Materials

Cell culture: Beta-TC-6 cells (ATCC), 25 mm^3 cell culture flask, DMEM (Thermo Fisher), FBS (Thermo Fisher), PenStrep, trypsin, 10 mL pipet, biosafety hood, personal protective equipment

Microfluidic device fabrication: silicon wafer, SU-8 2075 (MicroChem), SU-8 developer (MicroChem), Laurell WS-650-15B spin coater, photomask, UV exposure system, perfluorodecyltrichlorosilane, PDMS, hot plate, personal protective equipment

Methods

Cell culture: Beta-TC-6 cells were cultured according to common cell culture standards. Beta-TC-6 cell culture media consists of 85% DMEM by volume, 15% FBS by volume and 5mL PenStrep to mitigate bacterial growth. Once placed in the 25 mm^3 cell culture flask, beta cells require 12 mL of media to grow. The cells are grown in an incubator until confluent. At this point, they are either split into new flasks to continue growing or they are transferred to the microfluidic device for experimentation. Once transferred to the device, cells must be incubated in media in the microfluidic device to fully bind to the hydrogel sensor before the experimental live-dead assay is performed. The in-device incubator proved to be harder than initially expected and thus multiple live-dead assays were required to ensure cell conditions were favorable.

Microfluidic device fabrication: microfluidic devices are often fabricated using a polydimethylsiloxane (PDMS) soft lithography process. The first step in this process is to prepare a silicon wafer template on which to perform the PDMS soft lithography. SU-8 is spun onto the wafer using the Laurell spin coater according to desired MicroChem properties[19]. For this device, the SU-8 is spun for 10 sec at 500 rpm and 30 sec at 1050 rpm. The SU-8 is then soft baked onto the wafer for 5-7 minutes at 65C, then for 30 minutes at 95C. Next, the wafer is exposed to UV light for approximately 10 minutes. During UV exposure, a photomask, designed by previous student, is used to cover the wafer and thus selectively expose the SU-8 that is desired to stay. Figure 7 shows a portion of the photomask used for this gas gradient based experimentation.

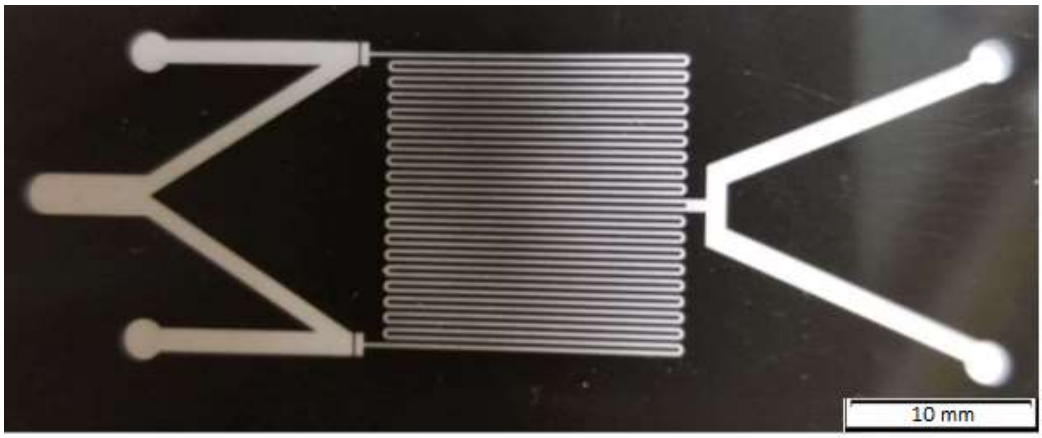

Figure 7. Photomask

The SU-8 covered wafer is heated once again post exposure, for 5 minutes at 65C, and then 12-15 minutes at 95C. The SU-8 is then developed in SU-8 developer for approximately 17 minutes in fabrication hood with fan on. This process removes the excess SU-8 that was not exposed under the UV light. The wafer is then washed with IPA after the design is fully developed. The wafer is then silanized using perfluorodecyltrichlorosilane in a vacuum desiccator for approximated two hours. This process increases hydrophobicity of the substrate and is essential as this particular device requires a very thin layer of PDMS that would be difficult to remove without this process.

Next, PDMS soft lithography is used to fabricate the device itself. PDMS is stored in the laboratory as two reagents, a pre-polymer solution and a curing agent, that must be mixed in a 10:1 ratio in order to initiate polymerization and the resultant curing process. For the gas gradient devices, only a thin layer of PDMS is needed and thus a spin coating technique similar to the one described above is used. First, PDMS is spun onto the wafer at 500 rpm for 10 seconds and 900 rpm for 30 seconds. This layer is cured at 85C for 20 minutes before a second coating is applied.

Once completed, the thin layer of PDMS is removed from the wafer and bound to a glass slide by activating surface O_2 radicals using a corona arc generator. A thicker layer of cured

PDMS (approximately 1 cm in height) is attached on top of this. This layer features a large cut out over the gas gradient portion of the device in which beta cells will later be cultured. This allows the cells to be directly affected by the gas gradient flowing beneath it (Figure 8).

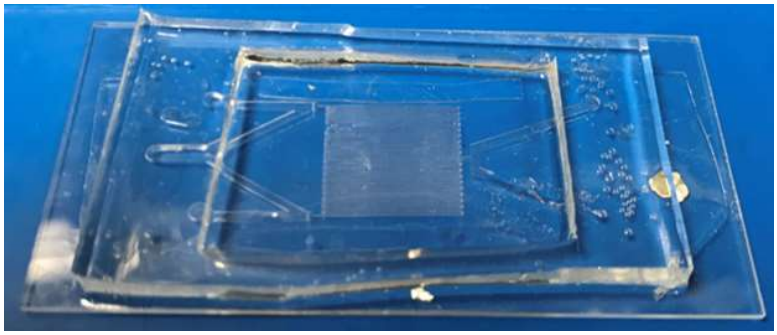

Figure 8. Completed Oxygen Gradient Device with Cell Culture Chamber

Chapter 3. An Introduction to Microfluidics and Shear Dependent Flow

Forces are everywhere in nature, even within the smallest blood vessels of the human body. Fluid flow within human body systems, or even in non-biological systems, is largely dependent on particle level forces. Flow is heavily affected by shear force, or the force acting parallel to a surface[20]. In fluid dynamics, this causes some particles to slip over one another, creating unique flow profiles. Generally, microfluidic networks behave according to Hagan-Poiseuille[21] law, creating a parabolic shaped profile in the direction of flow. This is due to the laminar flow of Newtonian (constant viscosity) fluids, which relies on a no-slip condition at the wall of the fluidic channel. The Hagan-Poiseuille equation[22] is as follows:

$$Q = \frac{\pi R^4 (P_0 - P_L)}{8\mu L}$$

where Q is the volumetric flow rate, R is the radius of the tube or vessel, $P_o - P_L$ represents the pressure drop across the tube, μ is the fluid viscosity and L is the length of the tube/vessel. It is clear mathematically that the radius has the largest effect on the volumetric flow rate under these conditions. In addition to constant viscosity, the flow must be laminar to meet these conditions. Laminar flow refers to flow that occurs in predictable, parallel layers as opposed to irregular, or turbulent flow. In terms of microfluidic environments, flow can be assumed laminar due to the low Reynold's number associated with these small geometries. The Reynold's number, represented by

$$Re_x = \frac{\rho V x}{\mu}$$

where ρ refers to fluid density, V refers to fluid velocity, μ to viscosity and x to the particular channel location of measurement, physically represents the ratio of inertial forces to viscous forces[22]. Here, we see that the Reynold's number is directly related to the fluid velocity, which will always remain low enough to produce laminar flow in microfluidic environments. As there is no longer concern with the possibility of turbulent flow, microfluidics provides a solid platform which allows users to focus on other aspects of the flow and/or fluid. One area of fluid dynamics of particular interest is the behavior of non-Newtonian fluids.

Non-Newtonian Fluid Flow

"Non-Newtonian" is the name given to a family of fluids which do not follow Newton's law of viscosity. A fluid can be considered Newtonian if the shear stress is directly proportional to the shear rate and does not change over time. Newtonian fluids can be summarized by the relationship:

$$\tau_{yx} = -\mu \frac{dv_x}{dy}$$

On the other hand, non-Newtonian fluids behave by thickening or thinning as the amount of applied shear rate increases[22]. Dilatant fluids become more viscous as shear is applied. Bingham plastics behave as if they were Newtonian, but only after a certain yield stress is reached (i.e. toothpaste). Pseudoplastic fluids become thinner as increasing shear is applied, such as ketchup. Casson fluids behave similarly to pseudoplastic fluids, but by definition contain a particulate phase. This particulate forms aggregates at small shear rates, but breaks apart as shear increases,

thus viscosity decreases over time. The Casson fluid model is the most relevant when considering fluid flow in biological systems[23].

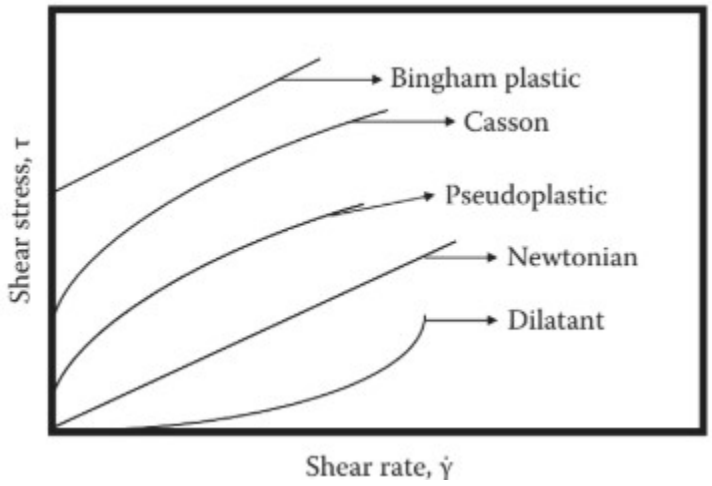

Figure 9. Non-Newtonian Shear Stress – Shear Rate Relationship[22]

Fluid Flow in Biological Systems

As mentioned previously, a large portion of microfluidics and this work is to adequately replicate body systems, fluid transport or organs within a "chip" model. For example, in the gas gradient device used to study the beta cells reaction to oxygen concentration, the aspect of fluid flow is removed by instead focusing on the oxygen gradient. However, in real life, oxygen is carried to the beta cells by means of hemoglobin contained in red blood cells. Human blood contains RBCs in abundance along with platelets and WBCs (white blood cells). The aggregation of RBCs at low shear rates are responsible for the consideration of blood as a Casson fluid. Casson fluids can be summarized by the following:

$$\tau^{1/2} = \tau_y^{1/2} + s\gamma^{1/2}$$

where τ_y is the yield stress and s is a constant. At high shear rates, γ, the Casson fluid will approach an asymptotic viscosity value[22]. For blood, this value is about 3 cP[24, 25, 26].

Blood Analog Fluids

Though not necessary for this particular study of beta cell characterization, it is important that any pumping mechanism we create for the study of microfluidics is capable of pumping biological fluids. To ensure the μTesla pump is proficient, all of the experiments carried out in Chapters 4-6 of this work were done using three different fluids.

The first fluid used for experimentation was distilled water with a viscosity of 1 cP and a density of 1000 kg/m^3. This does not serve as a blood analog fluid, but provides a necessary control fluid. Additionally, water, or fluids with similar properties such as cell culture media, are used frequently in microfluidic experiments.

The next fluid used for experimentation was a 3cP fluid was created by mixing water and glycerol according to standards determined by Segur et al[27]. and verified using an MVROC Viscometer. For reference, Figure 10 shows a sample readout provided by the viscometer. A solution of 36.4wt% glycerol delivered desired viscosity. The ρ of this solution was determined experimentally by

$$\rho = \rho_{water} * (\%_{water}) + \rho_{glycerol} * (\%_{glycerol})$$

Where the ρ value of glycerol is taken to be 1261 kg/m^3 for a final solution density of 1095 kg/m^3. This solution was necessary to mimic the viscosity of blood. Segur et al[27]. performed multiple experiments to determine the most comparable low-cost solution to blood while simultaneously minimizing biohazards.

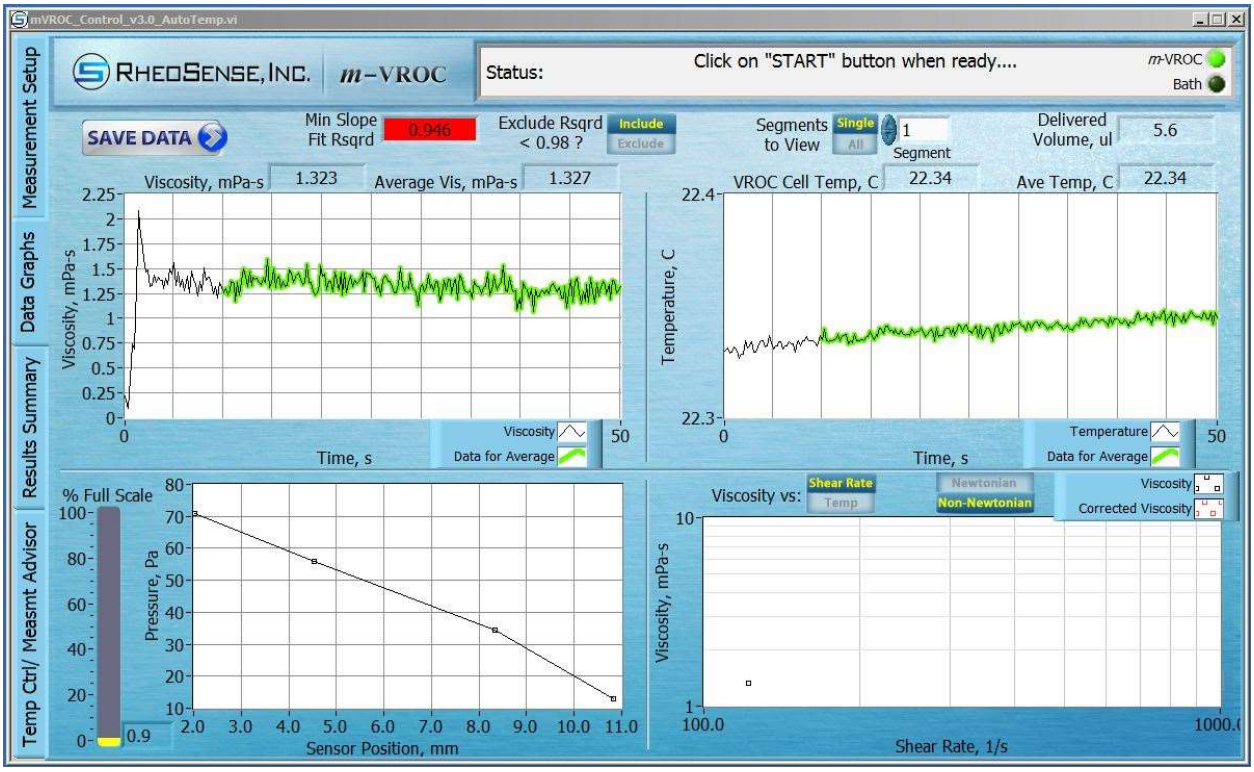

Figure 10. Sample MVROC Viscometer Read-out

Lastly, it was necessary to create a shear-thinning fluid to serve as a blood analog. Mann et al[28]. provides protocol for a shear-thinning xanthan gum-based analog. A 0.0375 wt% Xanthan gum in distilled water solution was prepared according to their protocol. The viscosity of the resultant fluid relative to applied shear stress (1/sec) was determined using the MVROC Viscometer. Four measurements per applied shear stress were averaged to result in Figure 11.

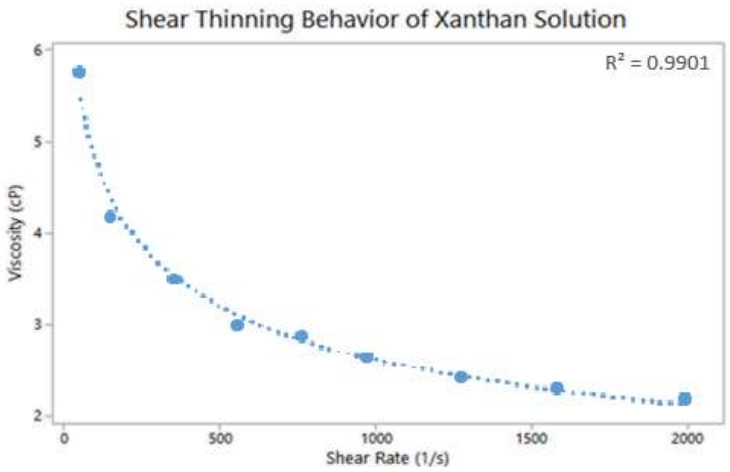

Figure 11. Shear Thinning Behavior of Xanthan Solution

As validated in Figure 11, the general behavior of the fluid is analogous to blood. Fournier[22] states that blood will approach an asymptotic limit of approximately 3 cP at shear rates higher than 100 1/sec. Our blood analog fluid exhibits a viscosity of 3 cP at approximately 600 1/sec, and later approaches a limit of about 2.18 cP. This may be attributed to a known drift seen in the viscometer technology.

It is unclear if this blood-analog is a true example of a Casson fluid, as Casson fluids rely on the formation of aggregates. Still, the results of experimentation using this fluid are very interesting to biomedical research.

Chapter 4. MicroTesla Characterization

Introduction

Fluid dynamic properties are well-defined in physics and nature, however, can be difficult to replicate on chip. In addition to challenges associated with fluids themselves, difficulty often arises as a limitation of the pumping mechanism. For example, a syringe pump may appear to operate seamlessly, but in reality, experiences microscale pulses in pressure output resulting in a less reliable flow profile. These microscale pulses introduce unaccountable shear forces into the fluidic network which in turn diminishes the system's likeness to a true biological system. It is worth noting that pumping systems of this precision do exist but are often unattainable to researchers due to their high cost. Thus, for the purposes of organ-on-a-chip research, it is desirable to create a reliable, pulseless flow source capable of pumping bodily fluids and their analogs.

The Tesla pump studied in this work was initially introduced by Nikola Tesla as his 1913 patented Tesla Turbine. As intended by Tesla, fluid would flow into the rotor unit by means of an inlet parallel to the rotor discs. The bladeless turbine would then accelerate the fluid flow inward by means of centripetal force, expulsing the fluid through the outlet perpendicular to the blades. The turbine, though patented by Tesla (Figure 12), never saw much commercial success due to the inability to maintain laminar flow conditions on his intended large-scale application of geothermal energy production[29, 30, 31]. Still though, over 100 years later, the Tesla turbine holds promise in other applications, namely microfluidics. As previously stated, microfluidic

environments are easily maintained within laminar flow, eliminating the unforeseen problems of Tesla. Thus by operating the Tesla turbine in reverse at a microscale, we are able to pump fluid directly into a microfluidic gradient while remaining within optimal flow conditions[32,33].

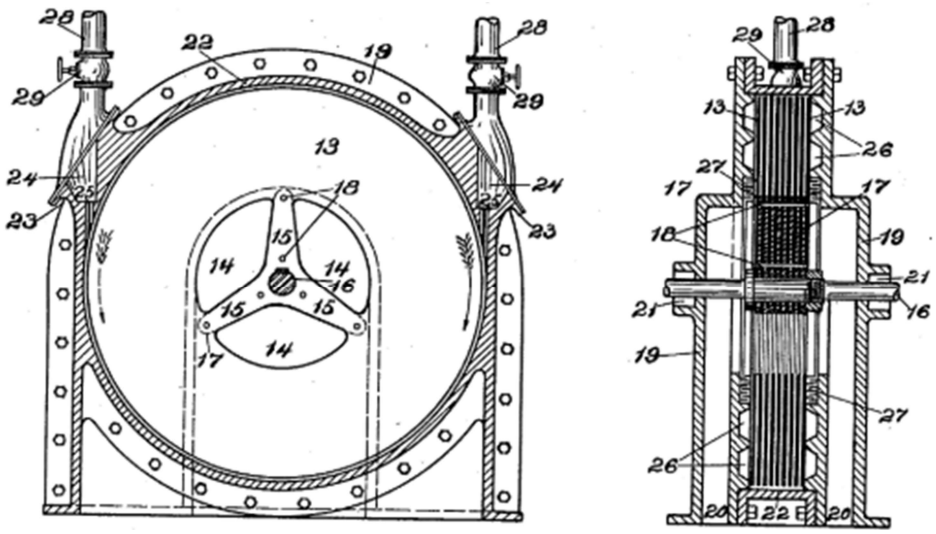

Figure 12. Tesla Turbine Patent Image

As intended by Tesla, the fluid would flow in through a side valve, label 28, and flow out through the center, 14. The propulsive forces are generated as the fluid is dragged in the very small spaces between the disks. When operated in reverse, the disks are magnetically coupled and are able to drive laminar flow in the spaces between the disks. Theories of fluid dynamics support this, such as the governing equation for steady incompressible laminar flow between disks[34]:

$$\frac{1}{r}\frac{\partial(rV_r)}{\partial r} + \frac{1}{r}\frac{\partial V_\theta}{\partial \theta} + \frac{\partial V_z}{\partial z}$$

where V is velocity and r, θ are the radius and angle as used in the cylindrical coordinate system. This equation can be simplified for our study by use of average velocities and imploring radial symmetry. It is also assumed that radial pressure gradients are negligible compared to angular forces. These assumptions reduce the governing equation to[34]:

$$\frac{1}{r}\frac{\partial(rV_r)}{\partial r} = 0$$

The laminar flow produced by the pump can be coupled to a microfluidic device and act as a power source.

Method of Fabrication

Previous work[34] in our laboratory realized a Tesla pump that was 2 cm in diameter, featured 6 disks, and a disk gap of 0.826 mm. For sake of clarity, that pump will be referred to as the first-generation Tesla pump. In this work, I have created a μTesla pump that is 1 cm in diameter, features 3 disks and has a disk gap of 0.412 mm. This was designed using the previous pump, and Tesla's original pump, as inspiration. The μTesla model was realized in CATIA and prepared for SLA-enabled 3D printing using Autodesk Meshmixer. Traditionally, .stl files are arranged in such a way that minimizes the amount of print time and material as discussed previously. In addition to this, prints are arranged to minimize any resolution-based defects. For example, when trying to print a straight line, it is best to arrange the line in a 2-dimensional linear fashion as opposed to introducing any angular components. At the pixel scale, the line y = 2 would appear flatter than y = x due to resolution limits of the graphics. This is replicated in any 3D print due to the pixel resolution restraints of the printer.

Instead of working to minimize this effect, the following work depends on exploiting this effect to increase surface roughness of the rotor discs without changing the CATIA model itself.

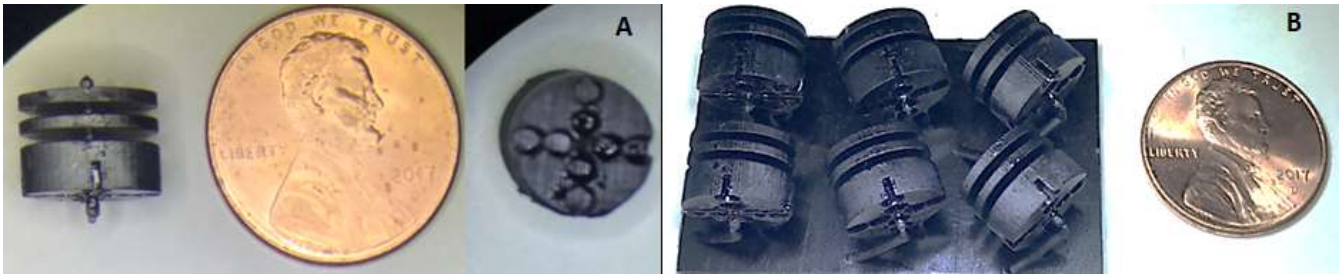

Figure 13. µTesla (A) Comparison of Single rotor to penny, close up of magnet storage, (b) µTesla rotors printed at in-plane angles of 0° (left), 22.5° (middle) and 45° (right) for induced surface roughness

As expected, the 0° rotors will feature a flat surface on the individual disks. By rotating the disk at 22.5° and 45° respectively, surface roughness is induced in the following way where measurements listed are in microns.

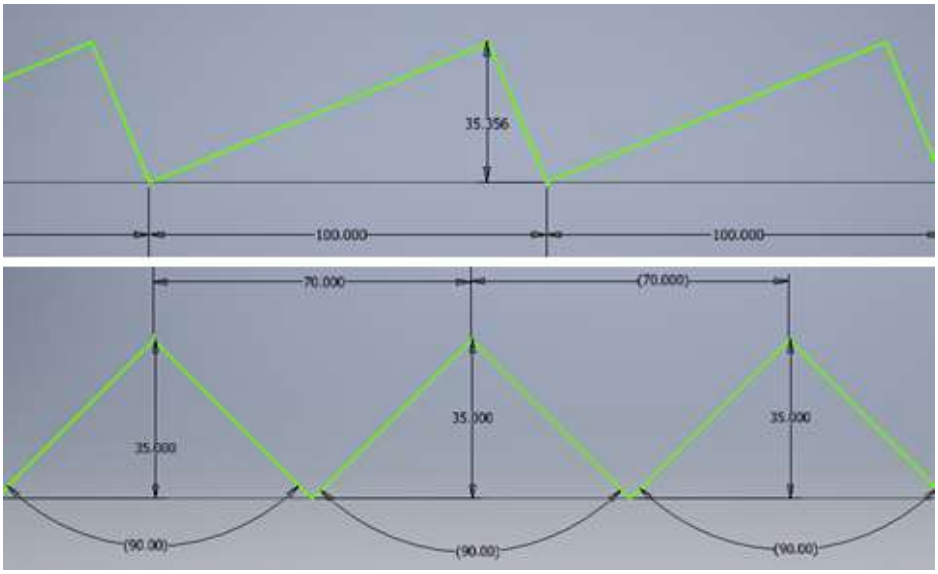

Figure 14. Induced Surface Roughness at (a) 22.5°, (b) 45°

Characterization of Rotor Surface

We sought to further characterize the rotor surface to validate our initial hypothesis that the print orientation of the rotor would have an effect on surface roughness. The surface roughness of the rotor discs perpendicular to the slice pattern was then measured using SurfJet SJ-210 technology (Mitutoyo). The act of slicing in and of itself will introduce a small,

immeasurable amount of surface roughness, but as this is seen in every print (regardless of print angle), it can be neglected.

Individual discs were removed from rotors for testing. Initially, both the top disk and the middle disk were tested but no significant difference was seen between the two. Conclusions were then drawn from the topmost disk for ease of experimental set up. After removing the top disk, any remnants of the central axis below the disk were sanded down to ensure that the disk lay flat when testing. The induced surface roughness direction was identified, and the disk was mounted to a glass slide. 3-4 disks were mounted using glue to a single slide while ensuring consistent directionality. It was ensured that the discs lay flat against the glue and as little glue as possible was used. Greater than 20 disks of each rotation from approximately seven different prints were tested. The roughness of each disk was tested four times – two times on each side of the central axis.

Results

The results generated by the Mitutoyo SurfJet SJ-210 technology include an evaluation profile, computed R_a, R_q, R_z values, and the raw data collected. A results readout for one of the 0° samples is included in Figure 15.

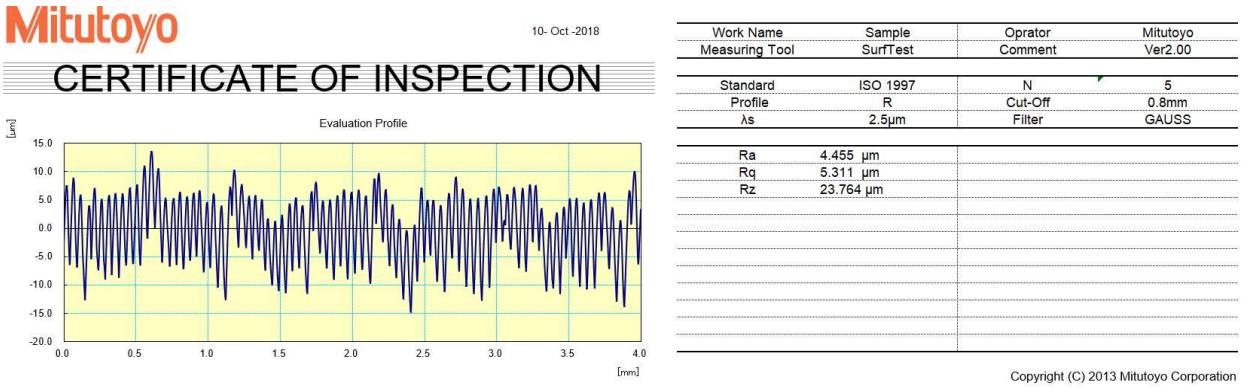

Figure 15. Example of SurfJet SJ-210 Output

R_a, R_q, and R_z represent three of the most common statistics reported from this type of test[35]. R_a represents the arithmetic average of the peak heights. R_z reports the greatest difference in successive measurements over the evaluation length. However, the value that is most interesting for our purposes is the R_q value, or the root mean square of the surface roughness. The R_q value reports the difference between the measurement's midline, or average, and the peak measurements. In other words, it reports the unidirectional amplitude. For the purposes of determining surface topology, the R_q value was doubled to account for the peaks and valleys of the surface. The summary of R_q values, not including outliers, is below.

	Average Rq (µm)	STDEV
0°	7.499	1.167
22°	7.813	1.139
45°	8.836	1.270

Table 1. Surface Roughness Data Summary

Discussion

While there is a clear trend in surface roughness measurements, it is not statistically significant with regard to the standard deviation. Furthermore, while significant differences in pump performance were observed (Chapters 5, 6), they do not follow the trend that this data set would suggest. The 22.5° pump inarguably performs the best. As this study of surface roughness could not produce results with statistical significance, the next question asked was, "why?"

As seen in Figure 14, the jagged edges created in 22.5° pump have a greater height than those in the 45° pump. When rotated at a 45° angle, each jagged edge is created by a single pixel. This is not possible for the 22.5° edges due to resolution limits. In this case, each jagged edge is created by two pixels. When solved mathematically, it is shown that the height of the point in the

22.5° is actually about 42 μm while the point in the 45° geometry is only 35 μm. Due to limitations of the AutoCAD Inventor software, the 22.5° height was modeled at 35.356 μm to better preserve the overall shape (due to geometric constraints, this geometry allowed for the other edges and angles to remain as close to theoretical values as possible. If set to 42 μm, the integrity of the other values would be lost).

The fact that the 22.5° points are indeed higher than the 45° points corroborates data generated in consequent studies (Chapters 5, 6). Upon further review, it can be asserted that the SurfJet technology did not pick up on the increased height for a few reasons. The aspect ratio of the 22.5° print is lower than that of the 45° print. While the overall height is 7 μm greater, the probe tip has approximately twice as long to reach this point. This means that the overall roughness is lower because there are less 22.5° peaks than 45° peaks on the surface. The distance between peaks on the 45° surface is 70 μm compared to 100 μm on the 22.5° surface. Over the 10 mm diameter of a disk, there are 42 more peaks on the 45° surface than the 22° surface. As the 22° surface has approximately 100 peaks, the 45° surface has nearly 50% more peaks.

In addition to this, the directionality of the 22.5° surface must be considered. For both the 0° surface and the 45° surface, directionality does not affect the measurement. No matter which end of the disc the measurement is initiated, the probe will encounter the same topology. This is not true of the 22.5° surface. As previously mentioned, each disk was measured perpendicular to the slice pattern starting from the same edge. However, in the case of the 22.5° surface, it is impossible to tell if the measurement was initiated from the high aspect ratio side or the low aspect ratio side. As the measurements of all the disks were taken to an average, this may have played a substantial effect in the results.

Chapter 5. Characterization of MicroTesla Flow

Introduction

The flow characteristics of the first-generation pump were determined by a previous research team. Upon realization of the μTesla pump, the experiments were replicated. Of course, the experiments performed were extended to each of the μTesla print angles. The following experiments were designed to showcase the μTesla's ability to produce a Poiseuille flow gradient capable of steady shear modulation.

Particle Velocimetry

This experiment seeks to establish the velocity profile generated by the μTesla pump when coupled to a microchannel by tracking the movement of microparticles within the channel.

Methods

The experiment was performed with each of the three fluids previously described – distilled water, glycerol solution, and xanthan gum solution. Fluorescent yellow-green polystyrene beads (2.0 μm mean particle size) provided by Sigma-Aldrich were added to the solution. The beads are stored as an aqueous solution of 2.5% solids. About 50 μl of fluorescent bead solution was added per 10 ml of fluid; however, the particle density is not particularly relevant due to the nature of the experiment.

The fluid was pumped from the μTesla pump through the microchannel. The 22.5° μTesla pump was used for this experiment as it has the greatest pumping capacity (Chapter 6).

The channel width is 550 μm. The μTesla pump was operated at 4000 rpm (linear edge velocity of 2.094 m/s) to maximize pump efficiency. Resistance was added using 1/16" ID tubing prior to the microfluidic network so that the velocity of the fluid through the imaging area was low enough to obtain high quality images. For reference, the previously determined linear velocity of 2.094 m/s can be approximated to a shear rate experienced in the 2mm ∅ tube by dividing the linear velocity by the width of the tube channel, or 0.002 m, resulting in a shear rate of 1047 1/sec. This means the Xanthan solution was likely exhibiting a viscosity of 2.18 cP during the experiments as shown in Figure 16.

Images were taken at 10 ms exposure. The location of the particles within the channel was recorded along with the particle length. By normalizing all collected data to μm measurements, the velocity of the particles could be determined by dividing the particle length by the 10 ms exposure time.

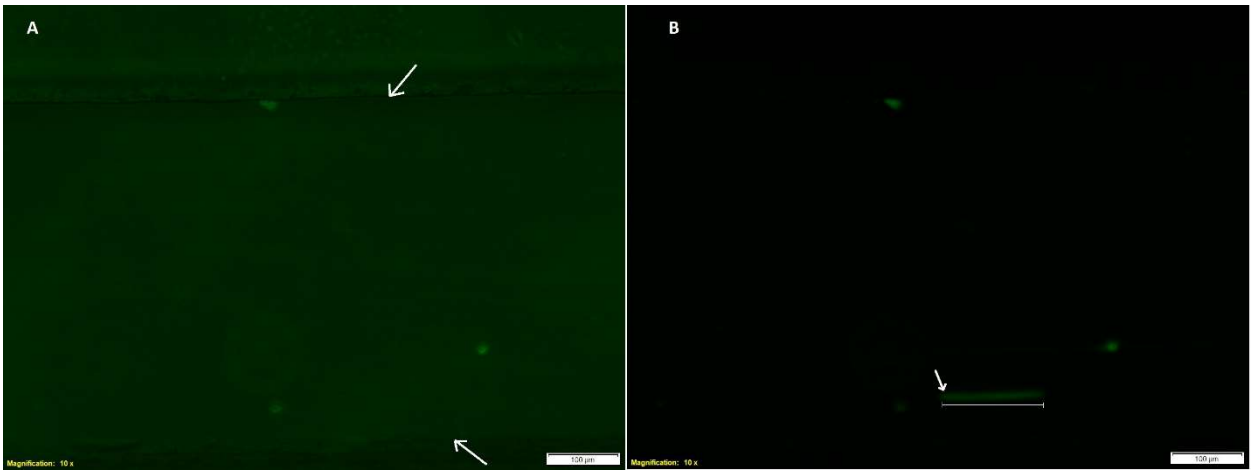

Figure 16. Microchannel Images (a) Image of channel with backlight to view edges of channel, (b) Darkfield image of channel with microparticle streak present

Results

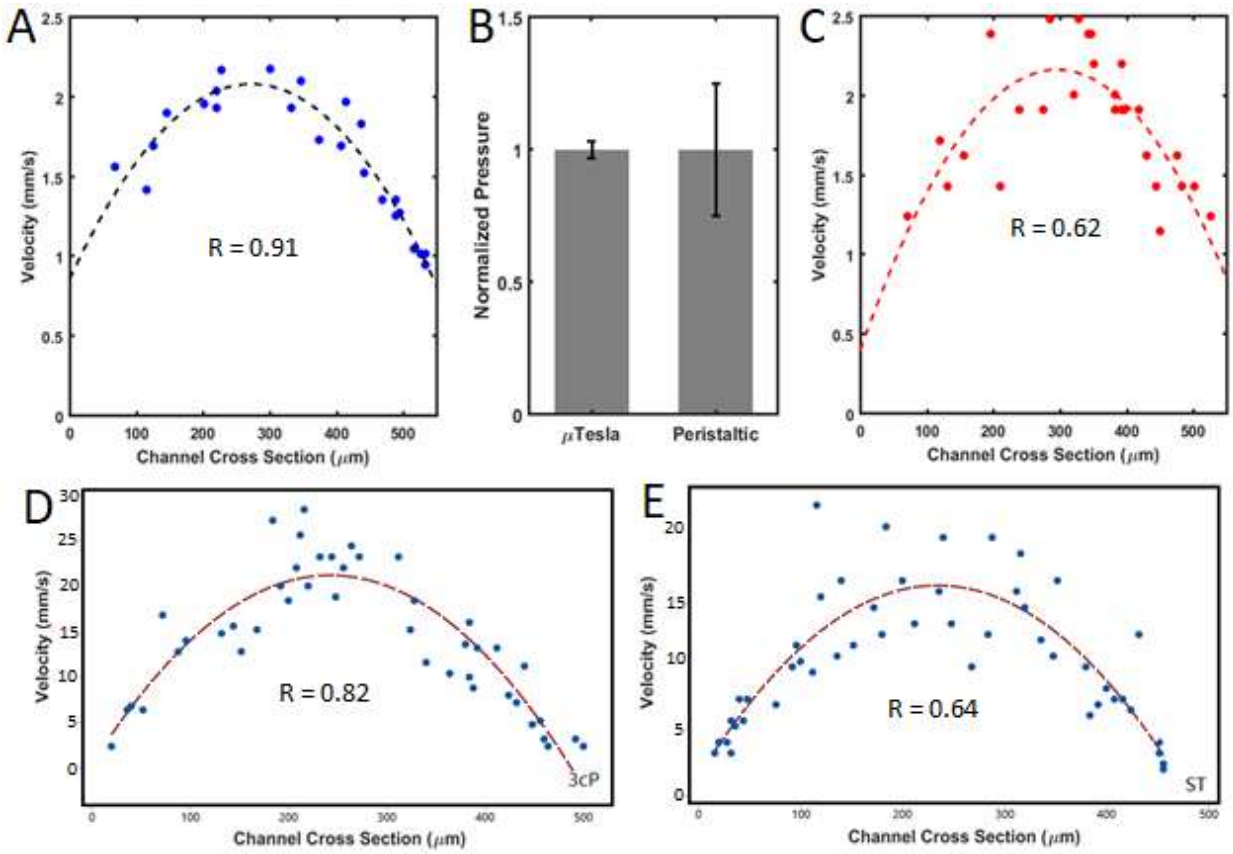

Figure 17. Determined Velocity Profile (22.5° Rotor), (a). µTesla flow profile at 1cP, (b). Comparison of normalized pressure, (c). Peristaltic pump flow profile, (d) µTesla flow profile at 3cP, (e) µTesla flow profile with shear thinning fluid

Figure 17 features the comparison of experimentally determined flow profiles. Each was fit to a parabolic line and the R value is given. Note that the experiments depicted by figure parts a-c were conducted using different equipment (results a-c were obtained using an AmScope microscope, d-e were obtained using an Olympus microscope). than parts d-e and thus the velocities obtained in mm/s are of different magnitude. The change in experimental set-up was due to a lack of resources following reorganization of the laboratory. The R value of the peristaltic regression is 0.62 compared with 0.91 and 0.82 by the µTesla pumping 1cP and 3cP fluid, respectively. The 1cP µTesla experiment was also repeated using the Olympus microscope. Not enough data points were obtained to constitute a new flow profile, however, the maximum velocity of the fluorescent beads in the 1cP fluid was higher than the maximum velocity of the

beads in the 3cP fluid. This is indicative of the expected results which would pump less viscous fluid faster.

Discussion

It is seen that the μTesla pumping mechanism achieves a parabolic fit greater than the parabolic fit of the peristaltic pump in all instances. The correlation value of the shear thinning fluid to the parabolic trendline, despite being higher than the peristaltic value, is very low (R = 0.64). This can be attributed to the fact that the flow profile for a shear thinning fluid is not truly parabolic. As previously discussed, shear thinning fluids are more accurately described as Casson fluids or by a non-Newtonian power law.

As previously discussed, Newtonian fluids are directly proportional to their viscosity whereas shear-thinning fluids take on the behavior of an apparent, or effective viscosity. This effective viscosity can be determined by a power law of the form[36]:

$$\mu_{eff} = K(\frac{du_z}{dr})^{n-1}$$

where K is the flow consistency index and n is the flow behavior index. As seen in Figure 18 from Dr. Eldridge[36], lower values of n will cause the parabolic profile to become flatter. Shear-thinning fluids often have n values less than 1 and thus can be expected to feature flatter profiles. In summary, the shear thinning fluid should not closely fit a parabolic profile as the actual expected fit was not attainable through this experimentation. Therefore, the R value is included as a point of reference but should not be used to draw any scientific conclusions on the shear thinning fluid.

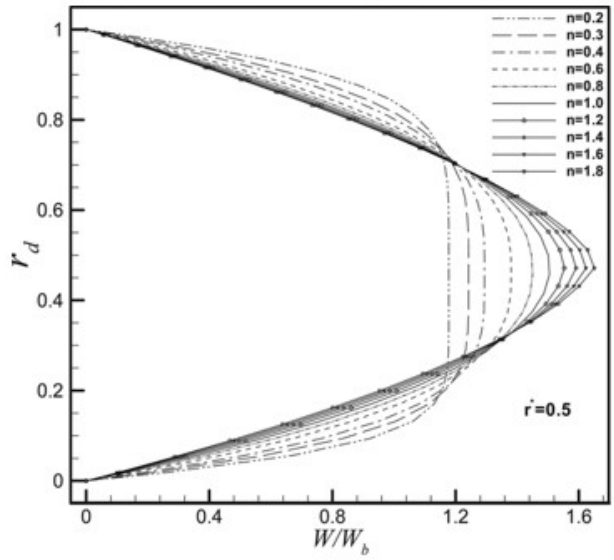

Figure 18. Shear Thinning Flow Profile[36]

Still, the μTesla pump achieved better correlation when pumping all fluids when compared to the Peristaltic pump. This not only validates the μTesla's compatibility as a flow source, but opens up the possibility of finely controlled shear. In terms of the experimentation with beta cells, controlled shear stress is required to simulate the beta cells response to shear forces in blood flow.

Computer-Aided Simulation via COMSOL Multiphysics

COMSOL Multiphysics is a simulation software capable of analyzing multiple physical phenomena at once. Even when only one physical phenomena is in question, COMSOL provides visually informative results to the user. The software was utilized to compare experimental results above with theoretical results, as well as gain useful information not readily available from physical experimentation.

Methods

The "laminar flow" module of COMSOL was used to perform these simulations. For simplicity, the simulations were performed in 2-dimensional space and assumed to be fully

developed, steady state (not dependent over time) flow. The channel walls were modeled as a no-slip boundary. 2-dimensional models of the space between the rotor disks were created in AutoCAD Inventor (Figure 14) and compiled into an AutoDesk .dxf file using AutoCAD (Figure 19). The channel width was modeled to mimic the disk gap, 0.412 mm and the channel length was modeled to the disk diameter, 10 mm. For reference, the hydraulic diameter (D_h), entrance length (L_h), and Reynold's number (Re) were considered at this time.

$$D_h = \frac{4A}{P} = \frac{4(0.000412m)^2}{(4 \times 0.000412m)} = 0.000412\ m$$

$$Re = \frac{\rho V \ell}{\mu} = \frac{1000\ \frac{kg}{m^3} \times 2.094 \frac{m}{s} \times 0.000412m}{0.001\ Pa \cdot s} = 862.73$$

Note that the values of ρ and μ for Newtonian fluids will cancel each other out and the Reynold's number becomes dependent solely on velocity and length.

$$L_h = 0.05 \times Re \times D_h = 0.05 \times 862.73 \times 0.000412\ m = 0.0178\ m$$

The 22.5° and 45° edges were modeled to the voxel resolution limitations as discussed previously.

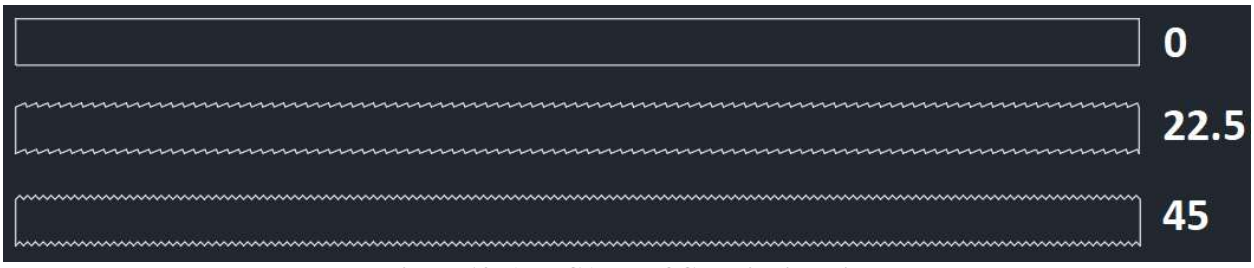

Figure 19. AutoCAD .dxf Compilation File

Once placed in COMSOL, a variety of studies were generated. The 1 cP fluid was modeled to a density of 1000 kg/m^3 and a viscosity of 0.001 Pa-s. The glycerol solution was modeled to a density of 1095 kg/m^3 and a viscosity of 0.003 Pa-s. Lastly, the Xanthan solution was not

directly modeled. Instead, the model for blood-mimicking solution was derived from experimental values of blood and modeled using the non-Newtonian Power Law input with a density of 1060 kg/m^3, m value of 0.01404 kg/(m-s), n value of 0.7885 and shear rate of 0.01 [1/s][37, 38, 39]. We were unable to properly model blood as a Casson fluid in this simulation.

The simulation performed seeks to validate the experimental results obtained from μTesla flow. The simulation was run with an entrance velocity of 2.094 m/s at each inlet. The outlet was defined by pressure output as experimentally determined in Table 3 (Chapter 6). Each channel was cut by 150 cut lines to analyze the flow throughout the entire channel.

Results

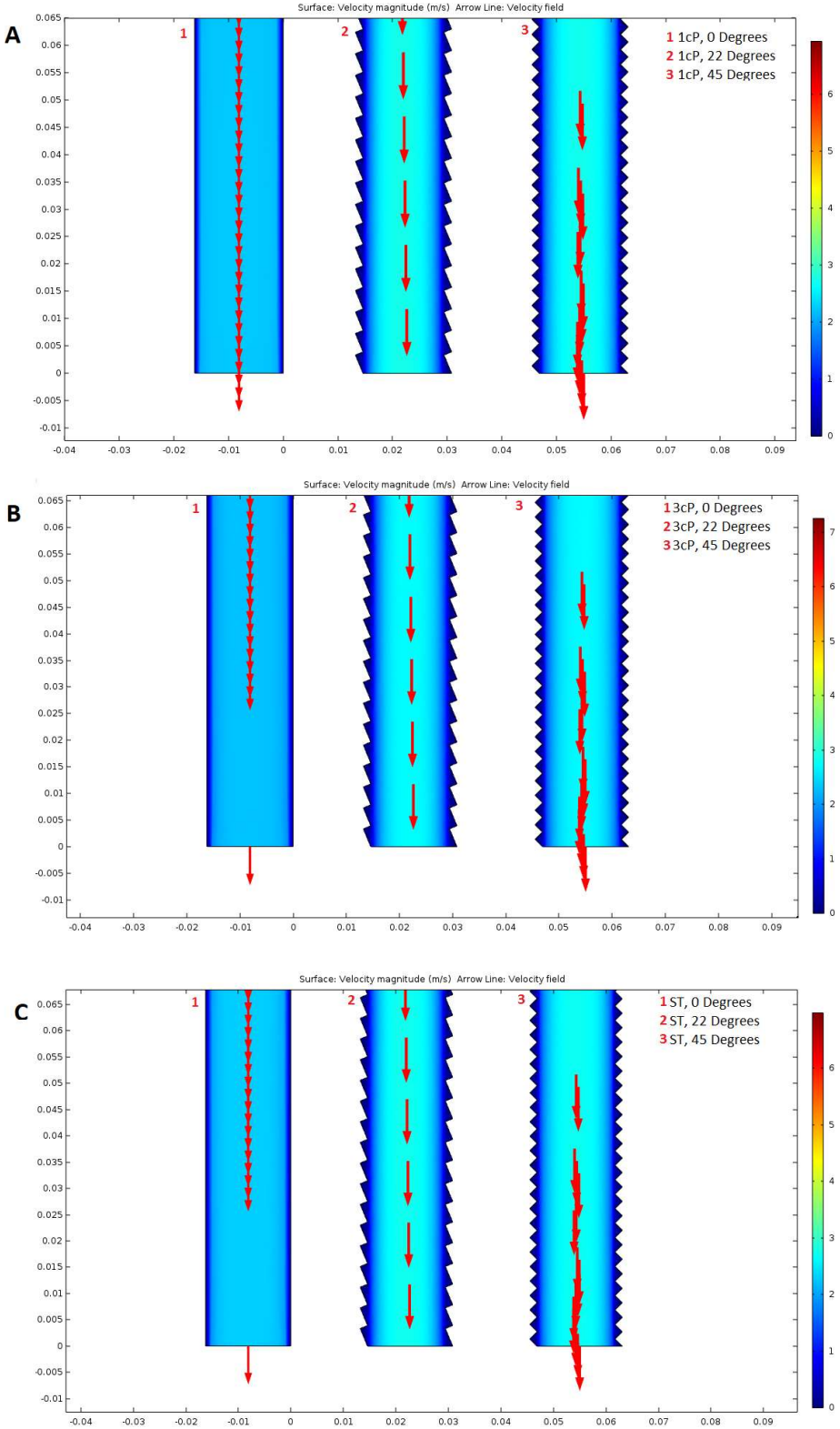

Figure 20. Velocity Magnitude in COMSOL Model (a) 1cP fluid, (b) 3cP fluid, (c) shear thinning fluid

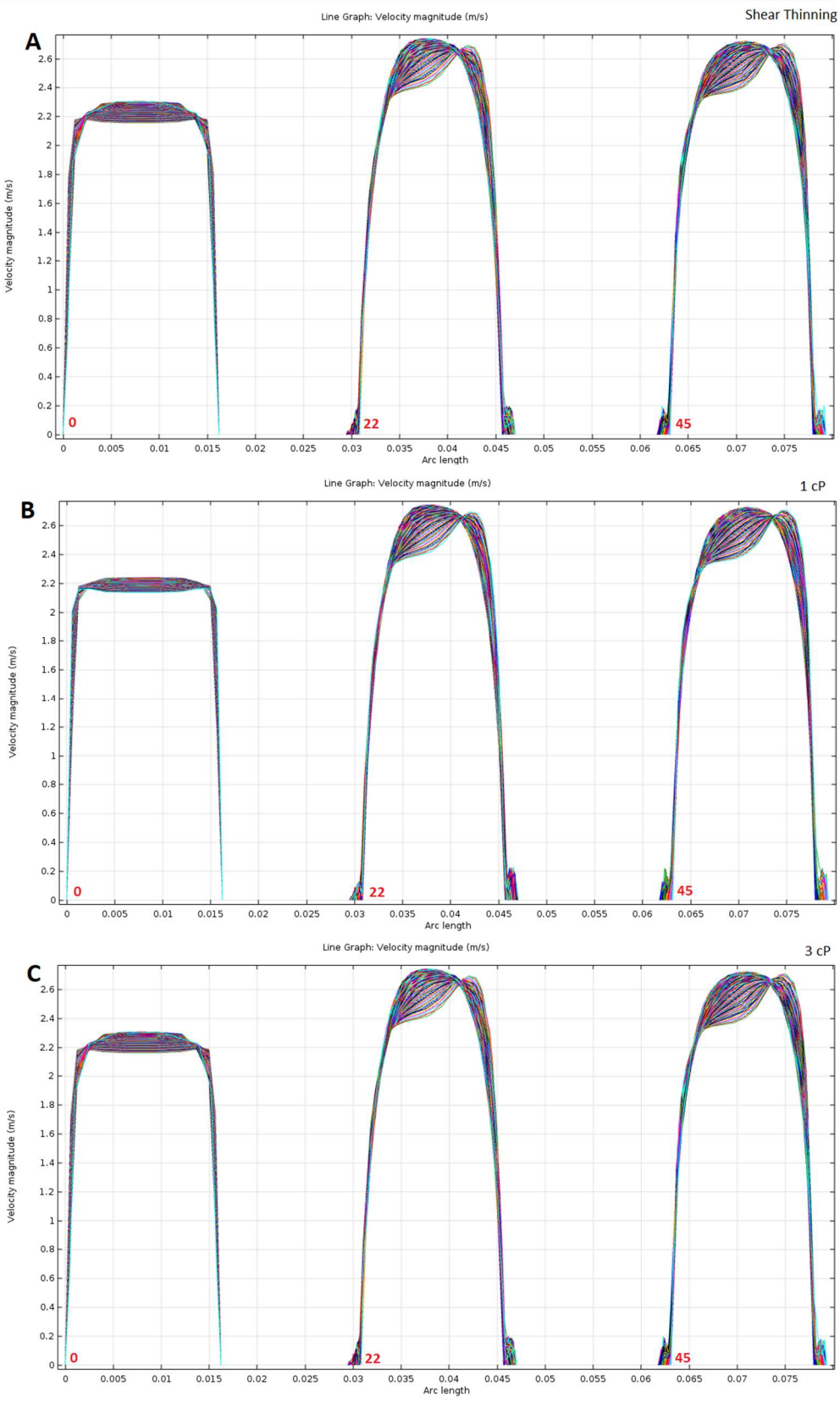

Figure 21. Velocity Profile from COMSOL Cut Lines, (a) shear thinning, (b) 1cP, (c) 3cP

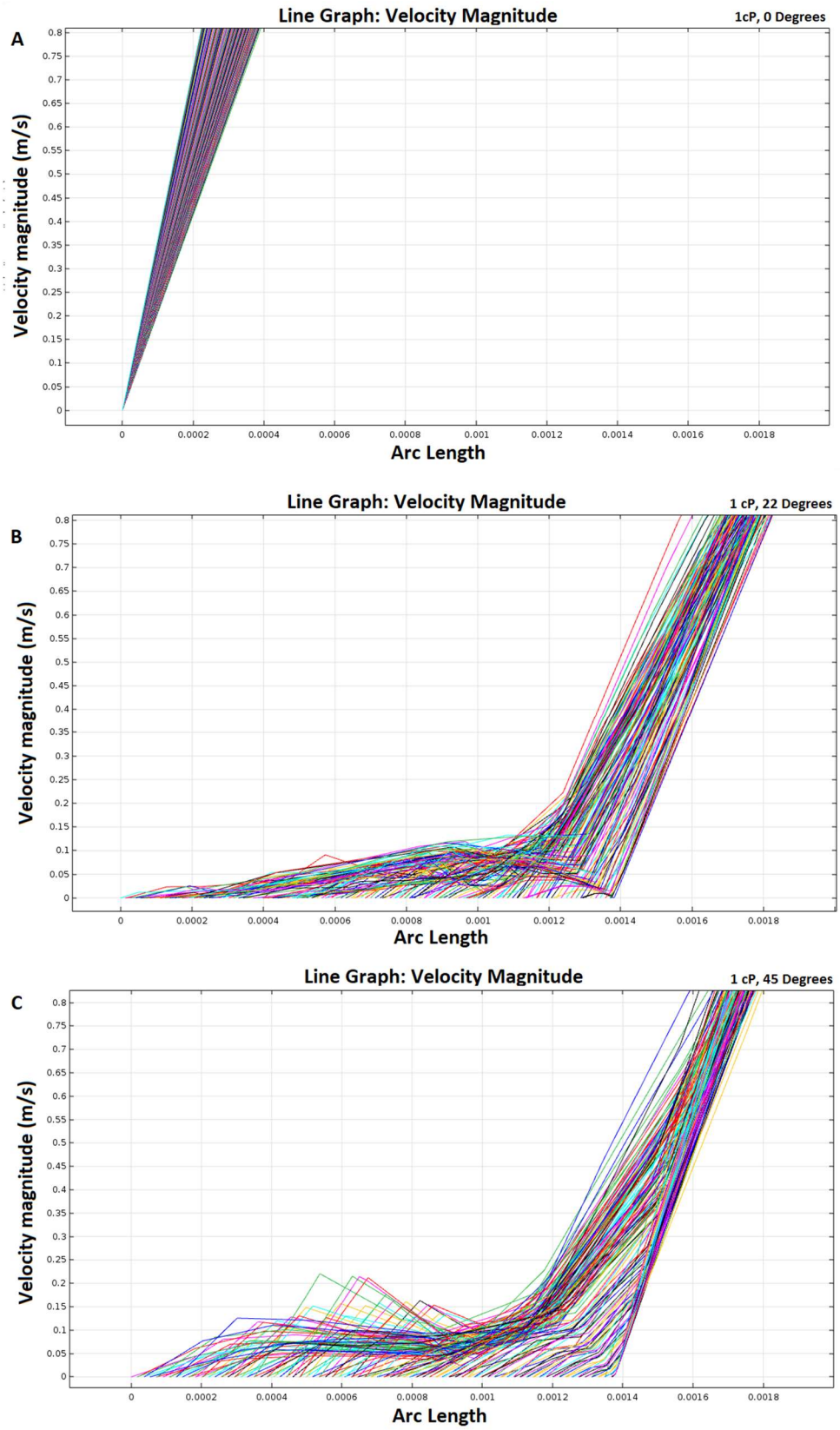

Figure 22. Left-hand Wall Slip Characteristics at 1cP, (a) 0 degrees, (b) 22.5 degrees, (c) 45 degrees

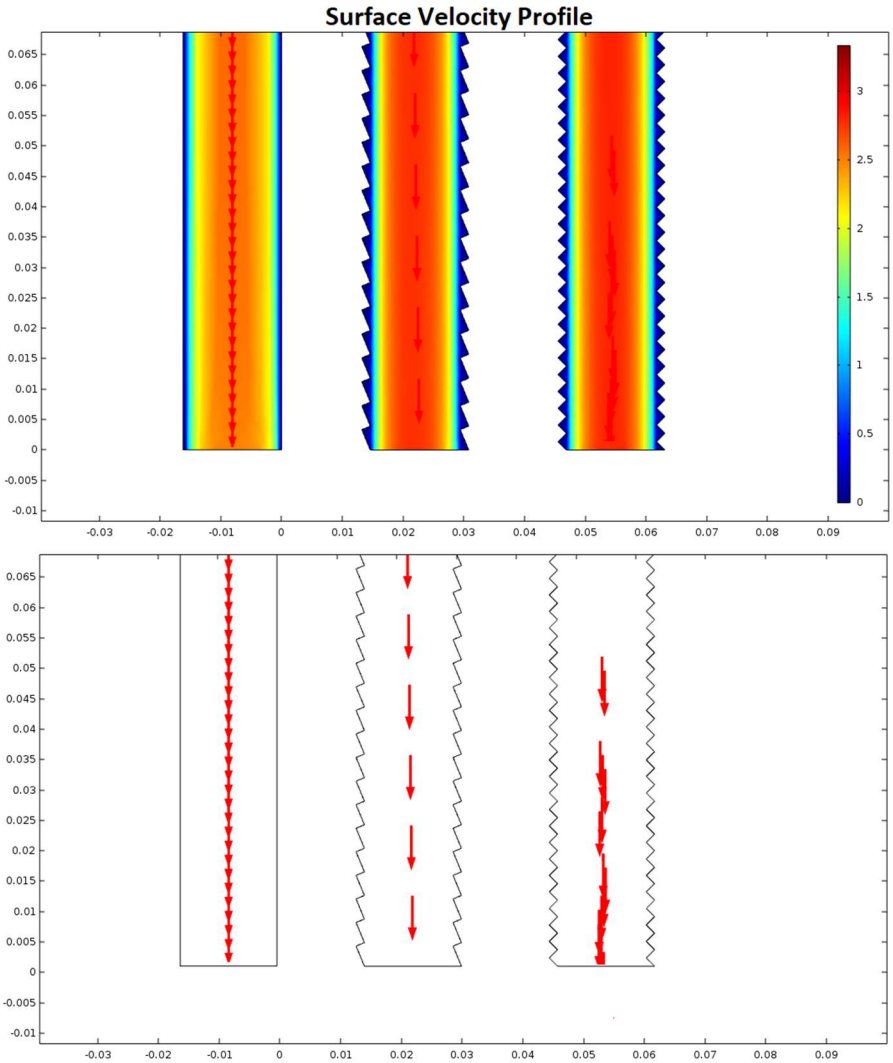

Figure 23. Velocity Profile with "Fine Mesh"

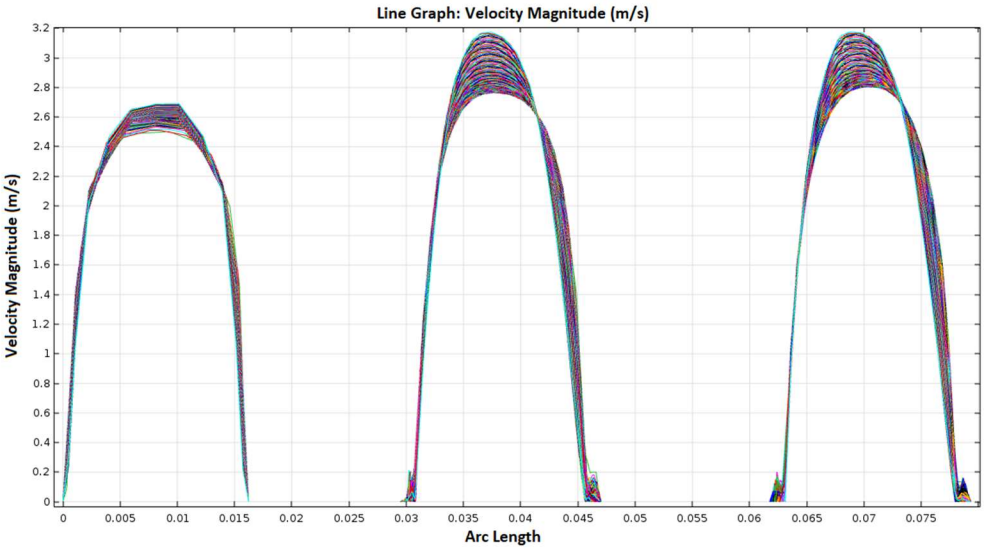

Figure 24. Flow Profile with "Fine Mesh"

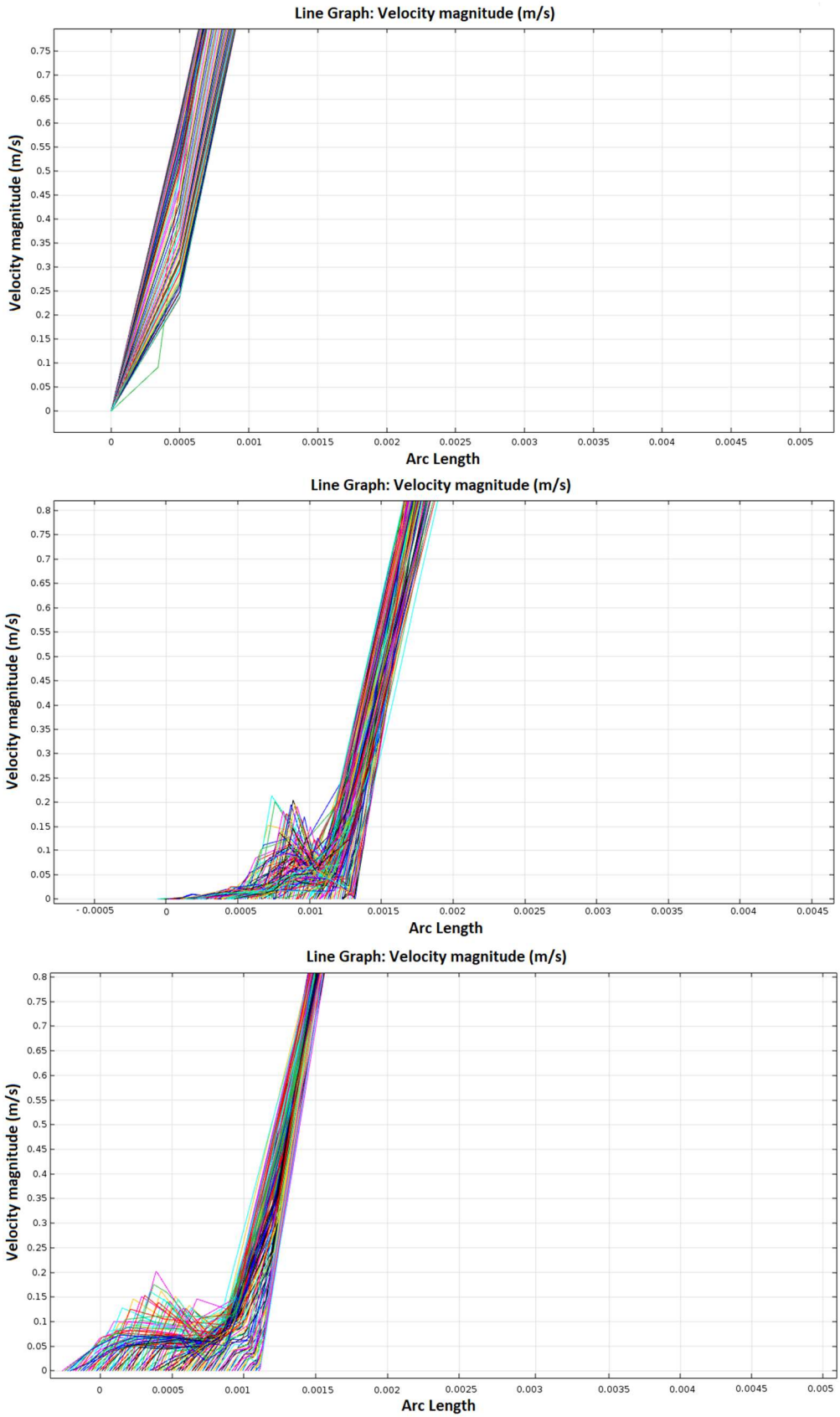

Figure 25. Left Hand Comparison of "Fine Mesh"

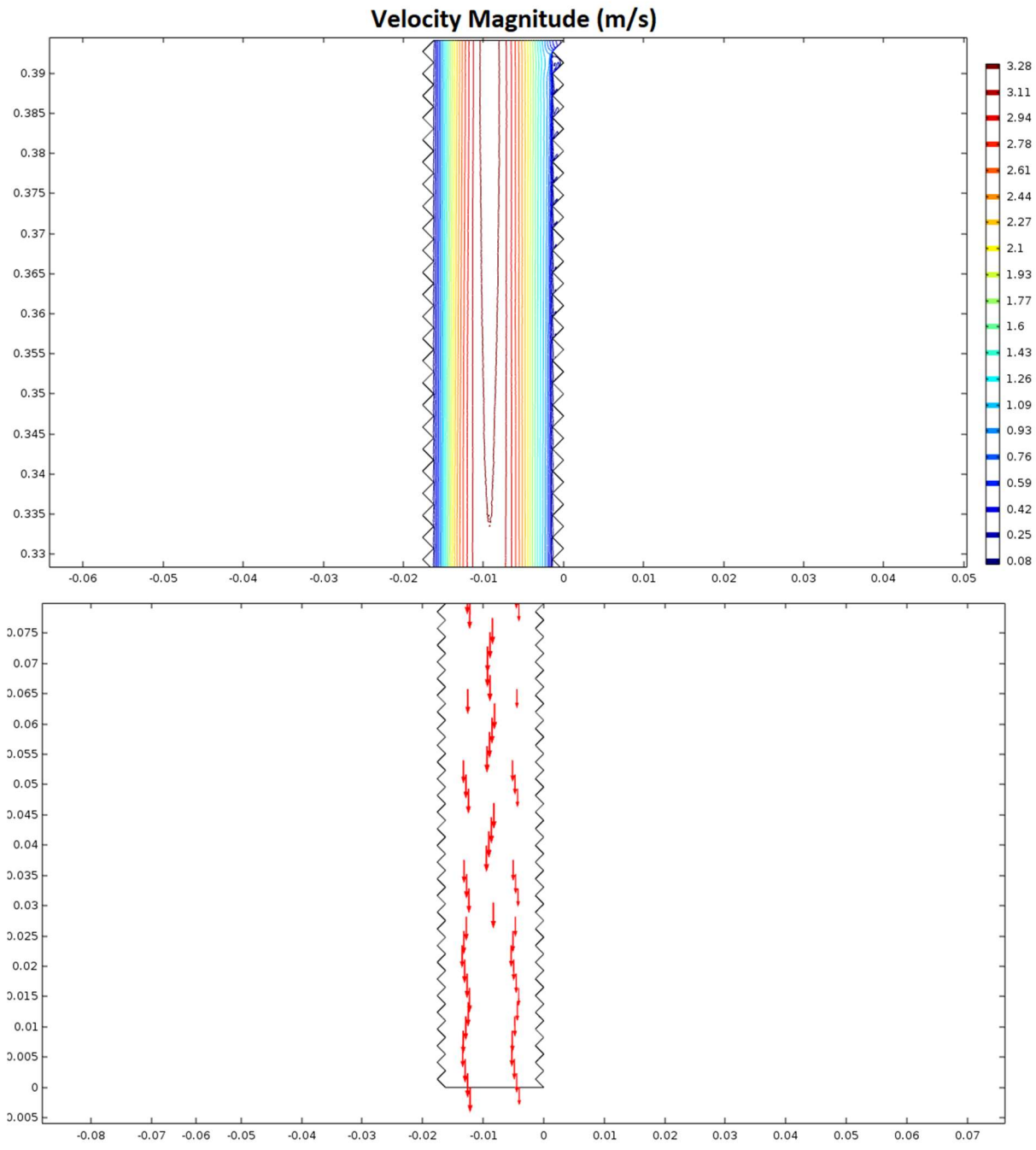

Figure 26. 45° Velocity Profile with "Finer Mesh"

Discussion

Figure 20 depicts the velocity magnitude of flow for all three fluids at their outlets. There is no major difference in the maximum velocity across the three different fluids, as expected by

the input velocity parameters. It can be seen that the 22.5° and 45° pumps have a higher maximum velocity than the 0° pump. Intuitively, this makes sense when considering the induced slip boundary at the channel edges. As depicted by the color representation in the channels, the dark blue region extends further into the channels of the 22.5° and 45° pumps than it does in the 0° pump. This means velocity is lower at the boundary. Effectively, the induced surface roughness, while not physically decreasing the overall ID of the channel, takes fluid flow away from the edges and pushes the flow into the middle of the channel. This will be explained further in this discussion, but the main takeaway from Figure 20 is the placement of the velocity arrows within the channels. The red velocity arrows represent magnitude of flow. Regardless of the fluid pumped, the velocity arrow magnitudes are larger in the 22.5° and 45° than the 0° pump, as expected. The interesting characteristic observed from this simulation is the shifting of the magnitude arrows in the 45° pump from the central line of the channel. In terms of fluid surface coupling, this indicates that perhaps the coupling is not as strong, and goes against our initial expectations.

Figure 21 validates the expected parabolic velocity profile of the fluids. The profile of fluids pumped with 22.5° rotors appears to achieve a slightly higher velocity. The profile of fluids pumped with 0° rotors appear much flatter than expected. This can be attributed to the mesh size associated with the 0° channel. When run simultaneously, only one mesh size is used (“normal”). The mesh results in a more accurate mesh for the 22.5° and 45° channels due to their extensive features. As seen in Figure 24, the accuracy for the 0° channel did increase when using a “fine” mesh, but solutions did not converge for any finer meshes.

Figure 22 compares in detail the left-hand wall characteristics of the velocity cut lines when flowing 1cP fluid. This data was pulled for each fluid, but results were identical and thus simplified here for brevity. Figure 22(a) features the expected result when considering a no-slip boundary condition. The velocity would be zero at the wall, and increase according to the parabolic flow profile (essentially linear at this small scale). Figure 22(b), (c) however show a slip of about 0.0014 inches, or approximately 35 μm. This is counterintuitive to our understanding of "no-slip boundary condition modelling" or "slip distance", which commonly refers to an exterior distance, as depicted in Figure 23.

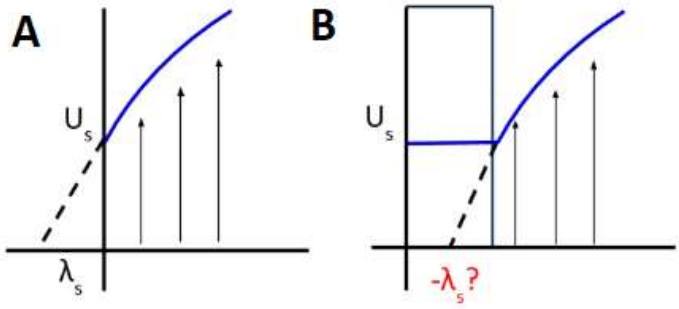

Figure 27. Slip Boundary Conditions, (a) expected, (b) μTesla

It is thus hypothesized that the induced texture of the μTesla rotors is contributing to slip distance within the channel itself[40]. A more detailed look into this phenomena is expected in future work.

To validate the disturbances in velocity flow observed in the 45°, Figures 23-26 represent studies done with finer mesh (on 1 cP fluid for brevity). As seen in Figure 23, the velocity profile is more well defined, but fluctuations in the velocity profile at 45° are still present. Figure 24 works to show that some of the aforementioned mesh-related abnormalities (compare to Figure 21) in the flow profile are smoothed out.

Figure 25 shows that the interior wall slip of ~35 μm is still present when using the "fine" mesh. However, in the original simulation (Figure 22), the maximum velocity reached within the slip region correlated to the channel roughness. The velocity in the 22.5° slip region reached .12 m/s whereas 45° reached .22 m/s. This was not seen in the "fine" mesh simulation and thus is assumed to be artificial.

More interestingly, Figure 26 shows velocity profile results of the 45° channel using a "finer" mesh. When the geometry was isolated, this more detailed mesh was able to converge. First, the velocity contours at the beginning of the channel are shown. At first, some fluid is entering the cavities, but within 0.05 inches (~1.27 mm) the velocity profile gravitates toward the center, completely avoiding the cavities. Furthermore, Figure 26 shows that the fluctuations in velocity at the end of the channel are still present, though decreasing in magnitude. Future simulations will seek to better understand this phenomena.

Chapter 6. Characterization of MicroTesla Output

Introduction

In addition to the flow characteristic of the μTesla pump, it was important to model the output pressure, or output capacity of the pump. For the purposes of this experiment, we considered no power loss within the pump itself.

Methods

2 mm diameter magnets were placed in the spaces in the bottom of the rotor (Figure 13 (a)). The rotor was then secured in a 3D printed housing specifically created for this experiment. The housing was used to ensure the pump remained upright, had an inlet perpendicular to the blades, and an outlet on the edge of the blades as described in Chapter 4. The rotor was magnetically coupled to a stir plate that operated at 4000 rpm as verified using an optical tachometer. 1/16" ID tubing was attached to the pump outlet and vertically aligned to a ruler. The ruler was used to measure the hydraulic head of the pump output in centimeters. When conducting the experiment, the pump was set so that fluid reached the 10 cm mark on the ruler and thus this 10 cm was subtracted from all measurements to determine a total change in height.

The stir plate was turned on and video footage of the fluid rise was recorded using an iPhone application that records video with .05 second precision. The video was stopped after the time reached 11 seconds. While we believe the ultimate pressure was reached by this point in the majority of the trials, it can not be asserted that the final pressure recorded is the true ultimate pressure of the pump.

Video footage was analyzed by recording the change in height every 0.5 seconds until 11 seconds was reached. The experiment was repeated in this way until there were 15 recordings of each pump-fluid combination.

To convert the previously determined linear velocity of 2.094 m/s to a shear rate experienced in the 1/16" ID tube, the linear velocity is divided by the width of the tube channel, or 0.002 m, resulting in a shear rate of 1047 1/sec. Figure 11 becomes asymptotic at approximately 2.18 cP (n = 4), meaning that the Xanthan solution was exhibiting a viscosity of approximately 2.18 cP when operating under 4000 rpm conditions.

0° rotor, 1cP fluid	22.5° rotor, 1cP fluid	45° rotor, 1cP fluid
0° rotor, glycerol solution (3cP)	22.5° rotor, glycerol solution (3cP)	45° rotor, glycerol solution (3cP)
0° rotor, xanthan solution	22.5° rotor, xanthan solution	45° rotor, xanthan solution

Table 2. Design of Experiment Analysis

The pressure output from the μTesla was determined as a function of the hydraulic head by:

$$p = \rho g \Delta h$$

where p represents pressure, ρ is density, g is the acceleration due to gravity (9.8 m/s^2) and Δh is the change in height.

Results and Discussion

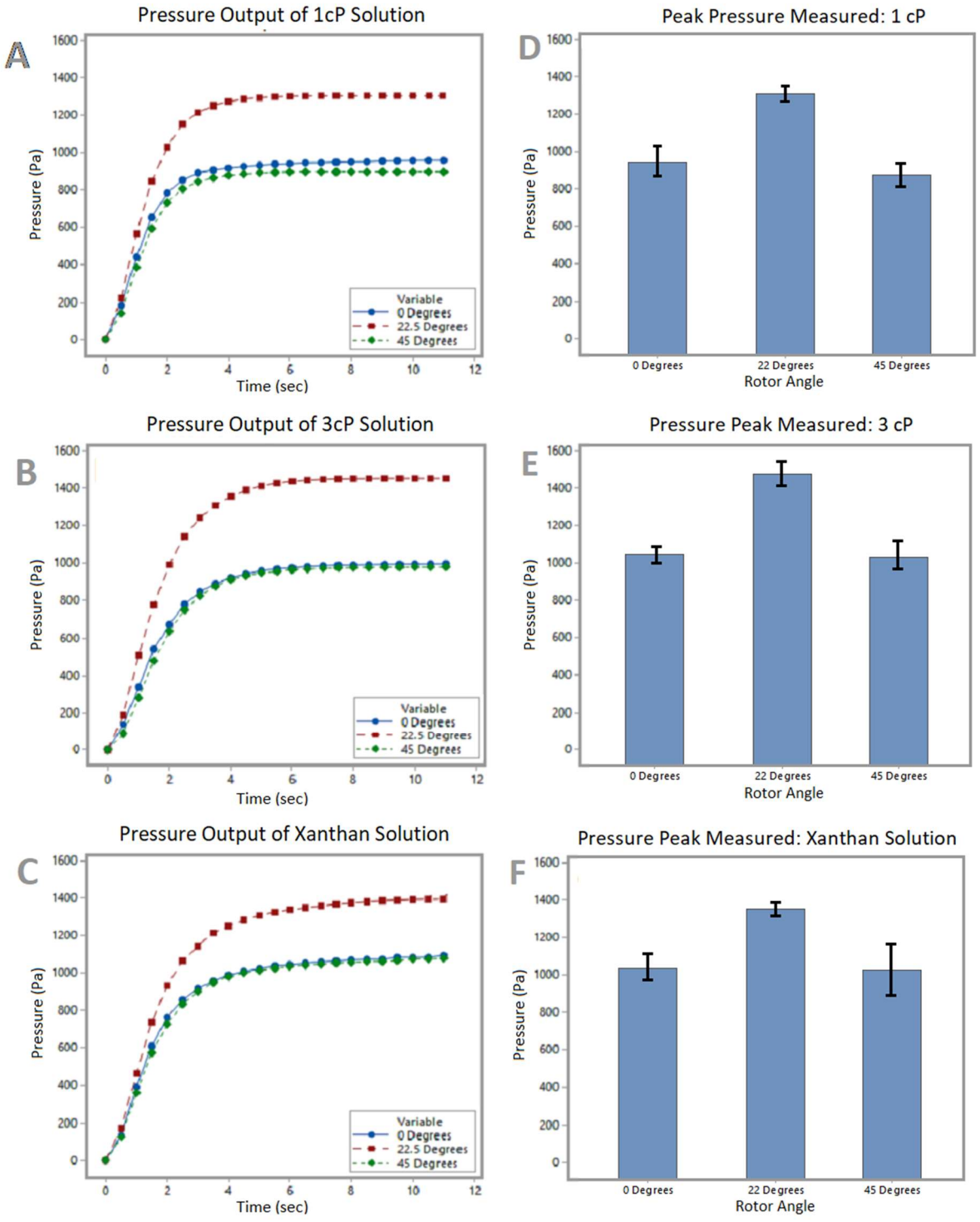

Figure 28. (a) Pressure Output of 1cP Solution, (b) Pressure Output of 3cP Solution (glycerol), (c) Pressure Output of Xanthan Solution

When pumping 1 cP fluid, the pressure produced by the 22.5° rotor was 36% than the second highest pressure, and 45.7%, 27.2% when pumping 3 cP and Xanthan solutions, respectively. Also worth noting is the general ability of the pump to reliably pump fluid. It is seen that the 45° rotor constantly produces the lowest pressure, however there is less of an overall difference in pumping capacity when pumping more viscous fluids. As shown, the pressure differences between the 0° rotor and 45° rotor are less than 20 (17.89 Pa and 16.45 Pa for 3 cP and Xanthan respectively) when pumping highly viscous fluids, but are greater at lower viscosity (61.41 Pa for 1 cP). The ultimate pressures recorded (Pa) are shown in Table 3 for numerical reference.

	1 cP	3 cP	Xanthan
0° rotor	958.44	997.27	1094.56
22° rotor	1302.75	1452.98	1392.56
45° rotor	897.03	979.38	1078.11

Table 3. Highest Recorded μTesla Pump Pressure Output

Figure 24 shows the pressure output of the various μTesla pumps using 1cP, 3cP and Xanthan solutions. The 22.5° rotor consistently produced more pressure regardless of fluid. For the 0° and 45° rotors, the Xanthan solution was the easiest to pump. This is corroborated by definition of a shear thinning fluid. Recall that Figure 11 shows that as the shear rate is increased, the viscosity of the Xanthan solution approaches 2cP. Each rotor is able to pump the 3cP solution better than the 1cP solution. It can be hypothesized that the Xanthan solution performs the best under these conditions because it has the advantage of a higher viscosity at the beginning of the trial (as the rpm is reaching maximum speed), but reduces to a more optimal viscosity as the rpm increases due to the shear-thinning behavior of the solution. Although this was not observed in the Xanthan solutions using the 22.5° rotor, the ultimate pressure values of the 3cP and Xanthan solutions were so close, this could be attributed to experimental error.

Perhaps the most impactful conclusion that is shown in these results is the statistically significant superior pumping capability of the 22.5° rotor. This is believed to be attributed to the directionality of the print, as discussed in Chapter 4. When printed at the 22.5° angle, the rotor discs on one side of the central axis will pixelate "upward" while the other side will pixelate "downward". This is not observed in the 45° print due to the aspect ratio of the pixels. Therefore, this result shows that not only can surface topology affect the fluid-surface coupling, the degree to which it does so can be very important. It seems that the 22.5° rotors act to drag the fluid while the increased (yet non-directional) topology of the 45° rotors create a type of microscale turbulence that actually degrades pumping capacity. Figure 20 visually represents this fluidic "rumbling" or generation of turbulence.

Also of interest is the comparison of the μTesla's pumping capacity to that of the first-generation Tesla pump. The first-generation Tesla pump developed by our laboratory produced output pressures of 253 Pa at 1200 rpm. This pump could not be tested at higher rpm due to decoupling of the magnetic forces. Noting the 20 mm diameter of the first-generation pump and the previously determined 2.094 m/s linear velocity test speed of the μTesla pump, using the relationship $v = r*\omega$ it is determined that the first-generation pump would have to operate at 209.4 rad/sec, or 2000 rpm to experience the same linear velocity at the disc edges. Using original data from the first-generation Tesla pump trials, extrapolation shows that the first-generation pump would be capable of producing 425 Pa when operated at 2.094 m/s linear velocity. This is less than half of the lowest 1cP value obtained with the μTesla pump (897.03 Pa on 45° rotor). This data matches the hypothesis that output is inversely proportional to pump size.

Chapter 7. Conclusions

This thesis highlights three main ways in which stereolithography-enabled 3D printing is capable of advancing research in biosensors, biomicrofluidics, and biotransport. The first way is through the development of MEMS devices for CNT proliferation and biomimetic compound eye models. This work was completed in collaboration with the laboratory of Dr. Cheng (Wayne State University) and future studies will utilize the stereolithography-enabled 3D printing information gained to better study the working mechanisms of compound eye models. The 3D print structure allows for the simulation of the ommatidia, previously unattainable in two dimensional studies.

The insight gained from the second and third sections of this thesis will advance biomicrofluidic and biotransport studies at the microscale. The μTesla, conceived from a need for a continuous flow source for cell culture studies, not only has the potential to serve in this role, but also provide a flow mechanism for studies requiring a highly accurate shear gradient. Future work centers on controlling shear stress over beta cells for diabetic pathophysiology studies. Moreover, the proven ability for the μTesla pump to flow blood analog fluids is an asset to these studies.

REFERENCES

1 Kirchmajer, D. M., and R. Gorkin III. "An Overview of the Suitability of Hydrogel-Forming Polymers for Extrusion-Based 3D-Printing." *Journal of Materials Chemistry B*, The Royal Society of Chemistry, 29 Apr. 2015, pubs.rsc.org/en/content/articlelanding/2015/tb/c5tb00393h.

2 Yoo, Seung-Schik. *3D-Printed Biological Organs: Medical Potential and* ...www.tandfonline.com/doi/pdf/10.1517/13543776.2015.1019466.

3 "Healthcare." *Materialise*, www.materialise.com/en/industries/healthcare.

4 "Customized Partial & Total Knee Replacements." *Conformis*, www.conformis.com/.

5 "Evaluation of Dimensional Accuracy and Material Properties of the MakerBot 3D Desktop Printer." *Rapid Prototyping Journal*, www.emeraldinsight.com/doi/full/10.1108/RPJ-09-2013-0093.

6 "The Ultimate Guide to Stereolithography (SLA) 3D Printing." *Formlabs*, formlabs.com/blog/ultimate-guide-to-stereolithography-sla-3d-printing/.

7 "High Resolution 3D DLP SLA Printer." *Kudo3D Inc.*, www.kudo3d.com/.

8 "Biomimetic." *Dictionary.com*, Dictionary.com, www.dictionary.com/browse/biomimetic.

9 Mnih, Volodymyr, et al. "Human-Level Control through Deep Reinforcement Learning." *Nature News*, Nature Publishing Group, 25 Feb. 2015, www.nature.com/articles/nature14236?error=cookies_not_supported&code=58b95fcd-7c90-470c-ac2f-def0ef99f688.

10 Abaci, Hasan E., et al. "Design and Development of Microbioreactors for Long-Term Cell Culture in Controlled Oxygen Microenvironments." *SpringerLink*, Springer US, 27 Sept. 2011, link.springer.com/article/10.1007/s10544-011-9592-9.

11 Moraes, Christopher, et al. "Organs-on-a-Chip: A Focus on Compartmentalized Microdevices." *SpringerLink*, Springer US, 8 Nov. 2011, link.springer.com/article/10.1007/s10439-011-0455-6.

12 Matthews, Benjamin D., et al. "Reconstituting Organ-Level Lung Functions on a Chip." *Science*, American Association for the Advancement of Science, 25 June 2010, science.sciencemag.org/content/328/5986/1662.full.

13 “Wayne State University.” *Dr. Mark Cheng - College of Engineering - WSU*, mcheng.eng.wayne.edu/.

14 Cagan, Ross. “Principles of Drosophila Eye Differentiation.” *Current Topics in Developmental Biology*, U.S. National Library of Medicine, 2009, www.ncbi.nlm.nih.gov/pmc/articles/PMC2890271/.

15 Land, Michael F. *The Optical Structures of Animal Eyes: Current Biology*. www.cell.com/current-biology/abstract/S0960-9822(05)00441-0.

16 Leary, James F. “Cytometry of Single-Cells for Biology and Biomedicine.” *Series in BioEngineering Essentials of Single-Cell Analysis*, 2016, pp. 235–255., doi:10.1007/978-3-662-49118-8_9.

17 Xi, Lei, et al. “Role of Tissue and Systemic Hypoxia in Obesity and Type 2 Diabetes.” *Journal of Diabetes Research*, Hindawi Publishing Corporation, 2016, www.ncbi.nlm.nih.gov/pmc/articles/PMC4932165/.

18 Unger, M.A.; Chou, H.P.; Thorsen, T.; Scherer, A.; Quake, S.R. Monolithic microfabricated valves and pumps by multilayer soft lithography. Science 2000, 288, 113–116

19 “SU-8 Negative Epoxy Series Resists.” *MicroChem*, microchem.com/Prod-SU8_KMPR.htm.

20 Pennsylvania State University. “What Is Fluid Mechanics?” *What Is Fluid Mechanics?*, www.mne.psu.edu/cimbala/learning/fluid/introductory/what_is_fluid_mechanics.htm.

21Richardson, S M. “Poiseuille Flow.” *THERMOPEDIA™*, www.thermopedia.com/content/1042/.

22 Basic Transport Phenomena in Biomedical Engineering. 2012. Ronald L. Fournier. 3rd edition, CRC pr.

23 Peters, Sara. “What Are Newtonian and Non-Newtonian Fluids?” *Crane's Fluid Connection Blog*, blog.craneengineering.net/what-are-newtonian-and-non-newtonian-fluids.

24 “Peristaltic Transport of Blood: Casson Model-II.” *Journal of Biomechanics*, Elsevier, 22 Mar. 2004, www.sciencedirect.com/science/article/pii/0021929084901404.

25 Chaturani, P., and V. Palanisamy. “Casson Fluid Model for Pulsatile Flow of Blood under Periodic Body Acceleration.” *Biorheology*, IOS Press, 1 Jan. 1990, content.iospress.com/articles/biorheology/bir27-5-01.

26 Walawender, et al. “An Approximate Casson Fluid Model for Tube Flow of Blood.” *Biorheology*, IOS Press, 1 Jan. 1975, content.iospress.com/articles/biorheology/bir12-2-02.

27 Segur, J B, and Helen E Oberstar. “Viscosity of Glycerol and Its Aqueous Solutions.” *ACS Publications*, pubs.acs.org/doi/abs/10.1021/ie50501a040.

28 Mann, David E, and John M Tarbell. *Flow of Non-Newtonian Blood Analog Fluids in Rigid Curved ...*www.researchgate.net/publication/20883837_Flow_of_non-Newtonian_blood_analog_fluids_in_rigid_curved_and_straight_artery_models.

29 Tesla, N. Fluid Propulsion. U.S. Patent 1061142 A, 6 May 1913.

30 Tesla, N. Turbine. U.S. Patent 1061206 A, 6 May 1913.

31 Steidel, R.;Weiss, H. Performance Test of a Bladeless Turbine for Geothermal Applications; Report No. UCID-17068;Lawrence Livermore Laboratory: Livermore, CA, USA, 1974.

32 Ho-Yan, B.P. Tesla turbine for pico hydro applications. Guelph Eng. J. 2011, 4, 1–8.

33 Hoya, G.P.; Guha, A. The design of a test rig and study of the performance and efficiency of a Tesla disc turbine. J. Power Energy 2009, 223, 451–465

34 Habhab, Mohammed-Baker, et al. “A Laminar Flow-Based Microfluidic Tesla Pump via Lithography Enabled 3D Printing.” *Sensors (Basel, Switzerland)*, MDPI, 23 Nov. 2016, www.ncbi.nlm.nih.gov/pubmed/27886051.

35 “Surface Roughness Terminology and Parameters.” *Http://Www.predev.com/Pdffiles/surface_roughness_terminology_and_parameters.Pdf*.

36 Eldridge, R. Bruce. “Non-Newtonian Fluids.” *CBE 150A Transport Processes*, University of California at Berkeley, www.cchem.berkeley.edu/cbe150a/index.html.

37 Irace, Concetta, et al. “Blood Viscosity in Subjects With Normoglycemia and Prediabetes.” *Diabetes Care*, American Diabetes Association, 1 Feb. 2014, care.diabetesjournals.org/content/37/2/488.

38 Skovborg, F, et al. “BLOOD-VISCOSITY IN DIABETIC PATIENTS.” *The Lancet*, Elsevier, 12 Sept. 2003, www.sciencedirect.com/science/article/pii/S0140673666912645.

39 Irace, Concetta, et al. "Empagliflozin influences blood viscosity and wall shear stress in subjects with type 2 diabetes mellitus compared with incretin-based therapy." *Cardiovascular Diabetology*, vol. 17, no. 1, 2018. *Academic OneFile*, http://link.galegroup.com/apps/doc/A546842218/AONE?u=lom_umichdearb&sid=AONE&xid=5810dafe. Accessed 26 Mar. 2019.

40 Niavarani A., Priezjev N.V. Rheological study of polymer flow past rough surfaces with slip boundary conditions. J. Chem. Phys. 2008;129:144902. doi: 10.1063/1.2988496.

41 J. Wang, Carbon-nanotube based electrochemical biosensors: A review, *Electroanalysis* 17(1), 7 (2005) https://doi.org/10.1002/elan.200403113